Student Thesis series INES nr 626

Predicting dust storm susceptibility: exploring control strategies with XGBoost models

Malgorzata A. Musur

2023
Department of
Physical Geography and Ecosystem Science
Lund University
Sölvegatan 12
S-223 62 Lund
Sweden

Malgorzata A. Musur (2023)
Predicting dust storm susceptibility: exploring control strategies with XGBoost models.
Master degree thesis, 30 credits in *Geomatics*
Department of Physical Geography and Ecosystem Science, Lund University

Level: Master of Science (MSc)

Course duration: *January* 2023 until *June* 2023

Disclaimer

This document describes work undertaken as part of a program of study at the University of Lund. All views and opinions expressed herein remain the sole responsibility of the author, and do not necessarily represent those of the institute.

Predicting dust storm susceptibility: exploring control strategies with XGBoost models

---

Malgorzata A. Musur

Master thesis, 30 credits, in *Geomatics*

Supervisors:
Pengxiang Zhao
GIS Centre, Department of Physical Geography
and Ecosystems Science, Lund University

Ali Mansourian
GIS Centre, Department of Physical Geography
and Ecosystems Science, Lund University

Exam committee:
Jean-Nicolas Poussart
GIS Centre, Department of Physical Geography
and Ecosystems Science, Lund University

Clarisse Kagoyire
GIS Centre, Department of Physical Geography
and Ecosystems Science, Lund University

Contents

List of abbreviations

Abbreviation	*Meaning*
ML	Machine Learning
TERB	Tigris-Euphrates River Basin
NDVI	Normalized Difference Vegetation Index
ME	Middle East
GEE	Google Earth Engine
RF	Random Forest
XGBoost	Extreme Gradient Boosting
LUC	Land Use Change
IOC	Intensity of Change
AUC	Area Under the Curve

Acknowledgments

I would like to extend my heartfelt gratitude to my family and friends for their emotional support and unwavering belief in me throughout the past six months. Their encouragement and constant presence have been invaluable in this journey.

I would also like to thank Pengxiang Zhao, Ali Mansourian, Hossein Hashemi and Amir Naghibi for their help, trust, and opportunity to play a part in the research project "AI in the Service of Socio-Politically Adapted Sustainable Dust-Storm Control in the Middle East", run at the Centre for Advanced Middle East Studies at Lund University. I am grateful for the opportunity to learn from the diverse perspectives and expertise within the group, and I greatly value the lessons and insights gained from our discussions.

Abstract

Dust storms are meteorological phenomena that occur in arid and semi-arid regions, causing harm to the environment and human health. The frequency and intensity of dust storms have increased in recent years due to climate change and human activities. In response, various dust storm mitigation strategies were introduced, including land use management, afforestation, and mulching. The existing research highlights various strategies for addressing the issue, however, there is a lack of specific regional modelling to evaluate their effectiveness.

This study simulates five dust storm mitigation strategies in three different regions in the Tigris-Euphrates River Basin (TERB) in the Middle East, and measures their effectiveness based on the decrease in dust storm susceptibility of the area. The strategies included increasing vegetation cover through expanding cropland and/or natural vegetation and expanding lakes through the partial opening of upstream dams. Extreme Gradient Boosting (XGBoost) machine learning algorithm was utilized for dust source susceptibility mapping. One model was created at pixel-level, which was the default for all simulations analysis. A second model was built to ascertain spatial influence on local areas following the simulations. The study found no effect of the *Spatial Model* on the neighbouring pixels following the application of the mitigation strategies.

The study's main finding was that all simulations decreased the areas' overall susceptibility to dust storms. The study revealed a spatial pattern where susceptibility increased and the response to mitigation strategies diminished progressively from the northern to the southern part of the TERB region. Further detailed analysis is recommended to consider region-specific factors in the region's response to mitigation strategies. Overall, this study provided insights into the dust storm control strategies' effectiveness. It has the potential to serve as a starting point for further research into modelling the effects and to aid in constructive and scientifically based mitigation planning.

1. Introduction

Dust storms are meteorological phenomena that commonly occur in arid and semi-arid regions. They are regarded as global disaster events, accompanied by strong winds and small particles lifted from land surfaces, obscuring visibility to less than 1 km (Middleton & Kang, 2017; Park et al., 2020). On the positive side, surface dust deposits provide micro-nutrients for both maritime and terrestrial ecosystems (WMO, 2022). But, on the other hand, they cause harm to human environment and physical condition, including damage to crops, removal of fertile topsoil and aggravating or causing health problems such as respiratory illnesses and cardiovascular disease (Middleton & Kang, 2017; Park et al., 2020). Additionally, they can affect air chemistry, climate processes, water cycle and soil characteristics among others. The effects of dust storms are not only experienced in and around the source areas, but also beyond the arid and semi-arid regions as desert dust can travel over large distances exceeding 1000 km (Maleki et al., 2021). According to Middleton and Kang (2017), all countries are indirectly affected due to numerous effects that dust storms have on the Earth system. It is therefore important to approach the study of this phenomenon in a transboundary context.

The study of dust storms has received significant attention over the last few decades due to their increased frequency and intensity in recent years caused by climate change (Salehi et al., 2021). Many researchers set out to understand how they form, their driving factors and how to best mitigate the sources and the impacts. Studies have used various remote sensing (RS) techniques to collect and analyse dust storm data, such as True Colour Composite image analysis, Normalized Difference Vegetation Index (NDVI), Normalized Difference Water Index (NDWI) and Aridity Index (AI) among others (Al-Dousari et al., 2022; Boloorani et al., 2020; Maleki et al., 2021; Middleton & Kang, 2017; Park et al., 2020). The subject matter remains highly relevant, as evidenced by the continuous influx of publications on the topic, such as the special issue of the Atmosphere journal entitled “Sand and Dust Storms: Impacts and Mitigation” released in January 2023. Awadh (2023) performed a review study which found that the annual amount of dust storms since 1960s has increased from 75 to 200. Dust storms are natural phenomena, but their frequency and intensity has additionally increased in response to human activities, such as soil surface disturbance, land degradation, desertification and mismanagement of water resources (Middleton et al., 2019, Salehi et al., 2021).

The relationship between the driving forces and dust storms is complex, mainly because of the variability of the factors. Climate and environmental conditions (including surface conditions and meteorological factors), adaptation ability in each region, as well as human activities all influence the formation and development of dust storms (Park et al., 2020). With that in mind, researchers have been looking into mitigation strategies that target at least one of the aforementioned factors. Thus far, previous research describes planned mitigation strategies without any concrete predictions regarding their effects. However, understanding, and visualising potential effects of dust source mitigation strategies could provide further aid in future policy and decision making.

This Master thesis is part of a project "AI in the Service of Socio-Politically Adapted Sustainable Dust-Storm Control in the Middle East" (Project), run at the Centre for Advanced Middle East Studies at Lund University. The reasoning behind this part of the study is to develop an approach to simulate dust storm control strategies and model how they affect the study areas' susceptibility. The study's findings have the potential to inform policymakers, decision-makers, and environmental agencies in developing effective measures to combat the adverse effects of dust storms. Furthermore, the utilization of machine learning techniques introduces methodological innovations enhancing understanding of these complex phenomena. By simulating and evaluating the impacts of dust storm control strategies, this study provides invaluable insights for future planning, risk assessment, and sustainable management of dust storms. Ultimately, the study's outcomes can contribute to the preservation of ecosystems, protection of public health, and the development of resilient societies in the face of increasing climate-related challenges.

1.1. Aim and Objectives

The aim of the project is to simulate dust storm control strategies using XGBoost machine learning models and to get an insight about the impacts of each strategy, based on the simulation results. To achieve this aim, the following objectives were developed.

Objective 1: Outline existing dust storm control strategies used in and around the study region.

Objective 2: Train XGBoost machine learning models to predict dust storm susceptibility, both including and excluding the neighbourhood effect.

Objective 3: Create simulations for dust storm control strategies.

Objective 4: Run the model on the most recent year available in the dataset and under selected dust storm control strategies, to evaluate the results.

Objective 5: Examine the impact of control strategies on susceptibility, and the incorporation of spatial effects on the outcomes of the simulations.

Hypothesis I: Application of dust storm control strategies will decrease the area's overall susceptibility to forming dust storms.

Hypothesis II: Incorporating the spatial effect in the XGBoost model will affect both directly changed and neighbouring pixels' susceptibility.

2. Background

In the last few decades, there was an increase in wind erosion and associated dust storms in different parts of the world including the Middle East (ME). The ME is responsible for approximately 24% of global dust emissions and is sensitive to climate and human-induced environmental changes (Ginoux et al., 2004). One region in the ME with a pronounced increase in new dust storm sources is the Tigris-Euphrates River Basin (TERB) (Boloorani et al., 2021) which is the focus of this study. Middleton and Kang (2017) warn that the reduction of water resources leads to the development of new hotspots, which is a potential reason for their increase in the TERB, as according to research by Boloorani et al. (2021) these are mostly located in recently dried up lake and marshland areas.

Maleki et al. (2021) highlights that the process of site selection for mitigation projects should include a comprehensive assessment of the fluctuations in water levels of rivers, wetlands, and lakes that are relevant to the area in focus. As shown by Papi et al. (2022), a 2007-2012 drought period in the ME led to a 52% decrease in the area's water bodies, sharp decline in groundwater resources and a 14-37% increase in sand and dust storms, as compared to the pre-2000 period. This research also highlights the issues in the south-eastern TERB, where the wetlands experienced the highest density of hydrologic dust sources, that were the consequence of anthropogenic activities upstream. Middleton et al. (2019) point to the fact that mitigating the probability of dust storms is not well understood, especially when related to human-induced factors such as overgrazing and diversion of water from sensitive areas.

As noted by Bremer (2016), scarcity of fresh water is a relatively new issue in the TERB, as the region did not experience any significant tension over the rivers' water before the first large dams were constructed in the 1970s. In 2018, Turkey completed the construction of a large dam upstream on Tigris River (Ilisu dam). It has been under increasing scrutiny since its planning stages due to the possibility of limiting water access in the rest of the TERB region, and adverse effects this might cause. A model of the worst case scenario effects of the Ilisu dam on the Mosul dam has been presented by Al-Madhhachi et al. (2020). The model predicts a reduction of up to 78% of the inflow into the Mosul dam if Ilisu dam does not take the downstream environmental impacts into consideration.

In 2015, United Nations General Assembly (UNGA) adopted resolutions entitled "Combatting sand and dust storms" that urges individual countries to address the challenges of dust storms through relevant policy measures. United Nations Convention to Combat Desertification (UNCCD) is helping countries develop policies with major focus on disaster risk reduction as is advocated by the Sendai Framework (Middleton and Kang, 2017, Aitsi-Selmi et al, 2015). Currently, out of all the TERB countries, only Syrian Law requires a transboundary environmental assessment on any major constructions planned within the country (Middleton & Kang, 2017).

2.1. Mitigation strategies

There are a few strategies that can be used to mitigate the creation of dust storm sources. One of the most applied strategies worldwide is afforestation, where trees and other regional climate appropriate vegetation are planted to reduce erosion and stabilize the soil. Park et al. (2020) point to the negative correlation between dust storm frequency and vegetation condition in Central Asia, drawing on successful implementations of vegetation restoration strategies in East Asia, such as the Great Green Wall in China. This research highlighted that the results of afforestation and restoration projects on the edge of the deserts were successful in decreasing the probability of dust storms occurring and were reflected in the range of the Normalized Difference Vegetation Index (NDVI). In Iraq, an initiative was undertaken in 2006 to address the expansion of desertification by establishing a green belt west of the Euphrates River, near Karbala city in central Iraq (Mutasher et al., 2021). However, the outcomes and the effectiveness of this undertaking remain undocumented in the literature available to the author. In southern Iraq, a dust storm hot spot is being targeted for mitigation efforts by the Kuwait Institute of Scientific Research. They are currently implementing a four-year afforestation strategy using green belts, as outlined by Al-Dousari et al. (2022). Another nearby hot spot, described in the study, is expected to achieve complete stabilization soon through the implementation of cultivation strategies.

In 2013, Iraq published a National Environmental Strategy and Action Plan (NESAP) that covered actions aimed at mitigating dust storms through addressing desertification. It is a sectoral national strategy document of Iraq, created in collaboration with the United Nations Environmental Programme, United Nations Development Programme and World Health Organizations (Ministry of Environment of Iraq, 2013). The Action Plan included, among others, sand dunes stabilization, creating green belts, proper management and conservation of water resources, land use management, and dust suppression techniques. Unfortunately, due to the political climate in Iraq between 2014-2017 the Action Plan was not implemented as planned. Currently, the Government of Iraq is working on updating their Action Plan, with the aim to cover years 2023-2028 (UNDP, 2022).

Iran has been a focal point for a significant portion of research in the ME concerning dust storm and desertification mitigation. Desertification has been recognised in Iran since 1930s, with first governmental measures set in 1950s (Amiraslani & Dragovich, 2011). Many dune stabilization initiatives were introduced, including mulching (covering soil with materials to minimize moisture losses), runoff control, windbreak establishment and increasing vegetation cover (Azoogh et al., 2018, Amiraslani & Dragovich, 2011). By 2015, 70,000 ha of Iran's Khuzestan province's sand dunes have been stabilized using the petroleum mulching-biological fixation (PM-BF) technique (Khalilimoghadam et al., 2015). This technique involves excluding the area after mulching followed by planting of specialist trees and bushes. Various soil surface stabilization experiments have been performed using different types of mulch to improve soil resistance to wind erosion. The types included polymers, petroleum products and biological products (Maleki et al., 2021; Namdar-Khojasteh et al., 2022). Azoogh et al. (2018) stresses that the application of petroleum mulching, which was the main type of mulch used in Iran, is not recommended for productive ecosystems. In recent years, combination of biological and mechanical treatments became more popular with the addition of windbreaks and shelter breaks that are typically used in agricultural areas (Middleton & Kang, 2017; Namdar-Khojasteh et al., 2022).

An important component of mitigation strategies is the selection of sites to be addressed. Maleki et al. (2021) proposed a method for prioritizing site selection that incorporates the physical and human variables interacting with sand and dust storms. Their approach considers six factors, including the identification of hot spots and the examination of additional physical variables such as vegetation cover and the presence of water bodies. The remaining three factors included changing distribution of dust storms, residential areas, and a soil texture map. By integrating these factors, their method considered the complex interaction between these variables and the occurrence of sand and dust storms.

Research by Salehi et al. (2021) classified sand and dust storm adaptation strategies into five categories. These include educational development, public participation, inter-sectorial coordination, institutional development, and environment preservation. The environmental protection class focuses on increasing the use of renewable energy, developing green space, and avoiding deforestation and desertification to combat increasing dust issues. On a regional level, they suggest protecting the environment through restoring ranges, forests and wetlands as well as returning land-uses and changing the cultivation by farmers. The research also showed that in Iran, some of the adaptive strategies were not based on scientific evidence as there is a disconnect between the authorities and the scientific community. Similar finding was presented by Amiraslani and Dragovich (2011) a decade earlier, which suggests that the disconnect still exists and needs to be addressed.

According to research by Papi et al. (2022), the accurate discrimination of different sources of sand and dust storms is a crucial factor in adopting optimal mitigation measures. The distinction was made based on whether the factors affecting the dust storm occurrence were natural, or anthropogenic in nature. One of the important points raised in the paper is that the hydrological cycle parameters, such as evapotranspiration, soil moisture, surface and ground water resources have a crucial role in the creation of the dust sources and should be investigated further.

The environmental, human, and political factors regarding dust and sand storms mitigation strategies are intertwined and complex. Proper assessment of the dust impacts and the strategies to address the problems is essential and called upon by researchers (Park et al., 2020). Thus far, mitigation strategies have not been simulated to model their effects on formation of dust sources. This type of simulation and modelling could potentially aid in developing mitigation strategies and help policy makers make informed decisions. This, however, poses another political difficulty as it would require international cooperation for policy making (Bremer, 2016).

2.2. Susceptibility mapping

As highlighted by Boroughani et al. (2020), susceptibility mapping can be considered the first step in dust management and mitigation. Since 2020, due to the complex relationships between the driving factors, researchers started applying and comparing multiple ML algorithms in dust storm susceptibility mapping with various conditioning factors. Compared models included statistical-based ML algorithms such as Weights of Evidence (Boroughani et al., 2020), ensemble learning models such as Random Forest (RF) (Boroughani et al., 2020, Pourhashemi et al., 2022, Boloorani et al., 2022, Naghibi et al., 2023, Jafari et al., 2022), Extreme Gradient Boosting (XGBoost) and Cforest (Gholami et al., 2020), Bagged and Multivariate Adaptive Regression Splines (MARS) (Gholami et al., 2020, Pourhashemi et al., 2022, Jafari et al., 2022). Hybrid models such as Adaptive Neuro-Fuzzy Inference Systems and Cubist (Gholami et al., 2020) and other types of ML models including linear Logistic Regression (Pourhashemi et al., 2022, Boloorani et al., 2022), Artificial Neural Networks (ANN) and Support Vector Machine (SVM) (Boloorani et al., 2022) were also considered.

The results of model comparisons showed that the best performing algorithm is the RF model reaching performance accuracy of 88% in the Boroughani et al. (2020) study and 92% in the research conducted by Pourhashemi et al. (2022). When RF model was not included in the comparison (Gholami et al., 2020), the best performance was achieved by the Cforest algorithm, which is another type of the ensemble learning model. In research by Naghibi et al. (2023) the RF algorithm was applied to four climatic periods with the highest performance accuracy reaching 87%. Boloorani et al. (2022) proposed an ensemble learning approach based on ANN, RF, LR Naïve Bayes and SVM models which proved to outperform each individual model. Individually, the best performance was recorded by the ANN (98.7%) and RF (98.4%) algorithms. Jafari et al. (2022) found similar results in their study, demonstrating that an ensemble of multiple ML models outperformed each individual model. Individually, RF was the best performing algorithm against ANN and MARS among others.

Ensemble learning methods have gained popularity in dust storm susceptibility mapping, with previous studies showing that RF outperformed many other models. Ensemble learning means that a model seeks better predictive performance by combining the predictions (XGboost, 2022). In the current study, a different ensemble learning method called XGBoost will be utilized. XGBoost combines predictions from multiple decision trees and has built-in handling strategies for missing data. It operates by boosting, meaning that it is iteratively adding decision trees to the ensemble and learning from past errors (XGBoost, 2022). XGBoost has demonstrated effectiveness in snow avalanche susceptibility mapping (Iban & Bilgilioglu, 2023) and landslide susceptibility mapping (Can et al., 2021), achieving performance accuracies of 97% and 96% respectively. These applications highlight the versatility of XGboost in addressing various natural hazard issues and support the choice of this ML algorithm in the current study.

As research by Naghibi et al. (2023) and Boloorani et al. (2022) focused on the TERB area, the results of their susceptibility mapping analysis were of high interest to this study. Naghibi et al.

(2023) performed a spatiotemporal analysis and noted that LUCs and water management strategies have a strong effect on dust storm susceptibility. They found that the highest susceptibility areas were located around dried up lakes and marshlands, even during the wet season. Susceptibility map for the TERB by Boloorani et al. (2022) shows regions most prone to dust storms are located in the east on the Iraq-Iranian border, and in the central-western TERB, by the Syrian-Iraq border. Medium susceptibility areas are present within the central TERB. Boroughani et al. (2020) highlighted that dust source areas were observed at poor vegetation cover, fine soil particles and flat areas. Jafari et al. (2022) additionally observed that mountainous areas and high soil moisture values indicate lower susceptibility.

2.3. Driving factors

The above studies included a variety of conditioning factors to train the models. The number of factors varied from six (Boroughani et al., 2020) to fourteen (Gholami et al., 2020), with the most factors in common including land use, lithology, slope, soil texture, NDVI, precipitation, elevation, and distance from river. Slightly fewer factors in common included wind speed, geomorphology, soil moisture and evaporation. Research by Naghibi et al. (2023) was performed by the Project members, on the same study area, utilizing the same dust sources dataset and several input variables as present research. The most important features in this study were elevation, NDVI, precipitation and soil texture. Jafari et al. (2022) found that evaporation, precipitation, and temperature were the most important factors affecting dust source formation. Land use was the most important factor according to Pourhashemi et al. (2023), followed by geomorphology, soil texture and NDVI. Boloorani et al. (2022) showed that soil moisture and vegetation indices were inversely related to dust storm occurrence. According to Gholami et al. (2020), the most important factor in dust storm formation was the wind speed, followed by land use, elevation and NDVI. The studies reveal that the most influential factors vary in each study. However, the topmost commonly identified factors include elevation, NDVI, precipitation, and soil texture. As highlighted by Jafari et.al (2022), there are no set rules for selecting variables affecting dust source formation and hence they may vary substantially across different studies.

3. Methods

3.1. Study area and data

3.1.1. Study areas

The overall focus of the study is on the semi-arid/arid TERB region in the ME in Western Asia (*Figure 1*). The area covers approximately 879,900 km^2 and spans across six countries including Iraq, Turkey, the Islamic Republic of Iran, the Syrian Arab Republic, Saudi Arabia, and Jordan. It contains high mountains in the north and north-east, and vast lowlands in the south and south-west. The two major rivers, Euphrates and Tigris, originate in the mountains of eastern Turkey, continuing to the Syrian and Iraq plateaux where they join near Qurna in Iraq, forming the Shatt Al-Arab River which empties into the Persian Gulf (FAO, 2009).

The region's water bodies are typically fed by either Euphrates or Tigris rivers. Notable lakes found within the central TERB region are Tharthar, Habbaniyah and Razzaza lakes. As mentioned by Boloorani et al. (2021), these three lakes along with Najaf and Hammar lakes, as well as Hawizeh, Central and Hammar marshlands are associated with the dust source locations identified in previous literature. As such, further focus of the study is predominantly centred around these hot spots.

Based on the frequency of documented dust sources between 2001 and 2020, existence of dust source hot spots, proximity to major rivers and proximity to urban centres, three areas were selected for conducting control simulations (*Figure 1*).

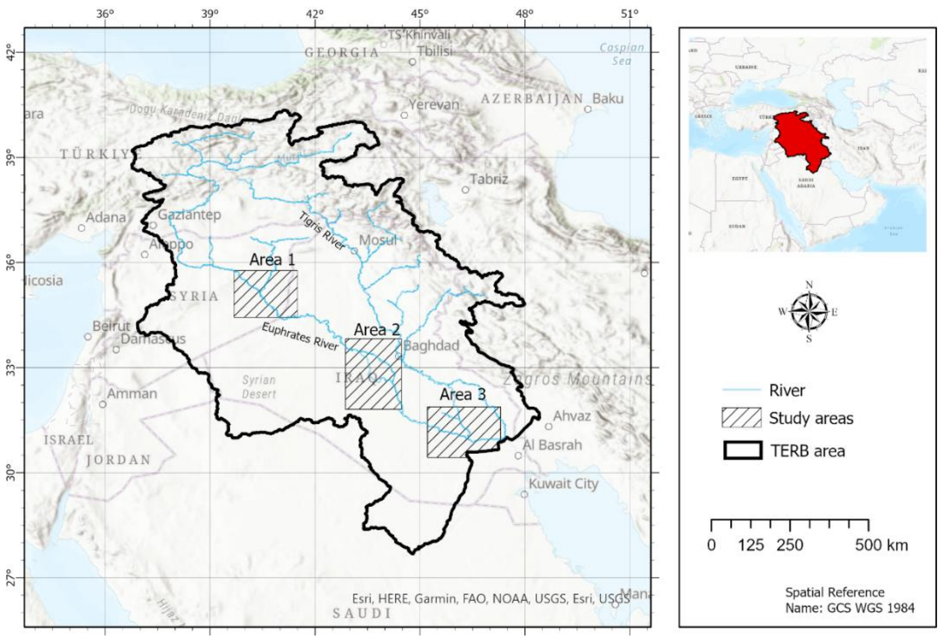

Figure 1. Map of the TERB region with highlighted three study areas and the presence of rivers.

Area 1, as seen in *Figure 2a*, encompasses the region of 30,300 km^2 in the central-northern part of the TERB region, predominantly consisting of Syrian territory and extending into two western provinces of Iraq. Two major rivers cutting across the area are the Euphrates and Al Khabour rivers, which are flanked by a series of small towns situated along their banks.

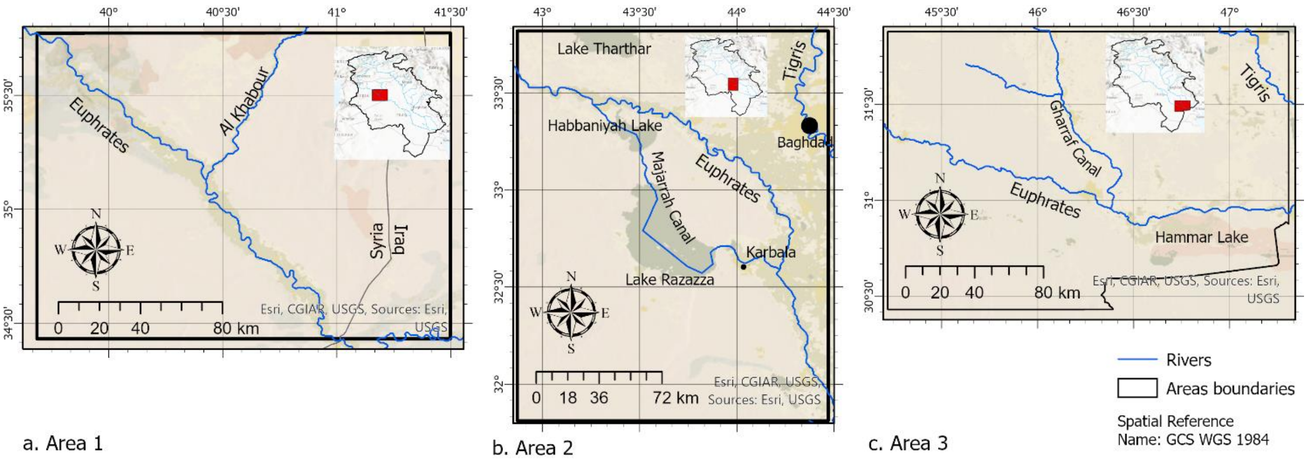

Figure 2. Study areas with their main rivers and lakes. a. Area 1, b. Area 2, c. Area 3.

Area 2 (*Figure 2b*), covering 39,694 km^2 of central Iraq in central TERB, encompasses the city of Karbala and the western portion of Baghdad. Euphrates river cuts across the area with its tributary Majarrah Canal serving as a connecting pathway between Habbaniyah Lake and Lake Razzaza. Tigris river is present in the northwestern part of the area. The northern section also includes the southernmost extremity of Lake Tharthar.

Area 3, shown in *Figure 2c*, encompasses 34,993 km^2 in the southern TERB. Euphrates River and Gharraf Canal cut across the area, feeding the Hammar Lake and the marshlands in the east. Tigris River is present in the northeastern part of the area. There are some urban centres and small villages along the riverbanks.

3.1.2. Data

To predict dust storm susceptibility, the XGBoost model incorporated fourteen driving factors as inputs, encompassing a time frame of two decades, specifically from 2001 to 2020. One of the reasons for selecting a 20-year dataset was the need to assume that future dust sources will be influenced by the same variables that caused them in the past (Boroughani et al., 2020). It was also crucial to ensure the appropriate size of the dataset, as the amount of dust sources per year varied between 2 in 2014 to 158 in 2008. The selection of inputs was guided by the review of previous research in the field, as described in the Background section. A summary of information regarding selected driving factors and the target variable is presented in *Table 1*. The base year for the control simulations was selected as 2020, which represents the most recent year within the dataset.

Table 1. Summary of the driving factors and the target variable used in the XGBoost susceptibility mapping algorithm.

Source	***Type***	***Factor***	***Data Type***	***Spatial data type***
DEM, (ASTER) Global Emissivity Dataset	Static	Elevation	Numerical	Raster
DEM	Static	Slope	Numerical	Raster
DEM	Static	Aspect	Numerical	Raster
DEM	Static	Profile curvature	Numerical	Raster
DEM	Static	Plan curvature	Numerical	Raster
DEM	Static	Curvature	Numerical	Raster
River vector file, HydroSHEDS	Static	Distance from river	Numerical	Raster
OpenLandMap Soil Texture Class	Static	Soil texture	Categorical/ Numerical	Raster
GSSM1km dataset	Dynamic	Soil moisture	Numerical	Raster
PML_V2 product	Dynamic	Soil evaporation	Numerical	Raster
UMD land cover data	Dynamic	Land cover	Categorical/ Numerical	Raster
MOD13A2.061 product	Dynamic	NDVI	Numerical	Raster
GPM v6 product	Dynamic	Precipitation	Numerical	Raster
NDVI dataset	Dynamic	Lake size	Binary/ Numerical	Raster
True Colour Composite images	Target/ Dynamic	Dust sources	Binary	Vector

Most of the factors selected for this study were used by the Project team members in the Naghibi (2023) research paper. Additional inputs, such as soil moisture, land cover, lake size and soil evaporation were added to aid in fulfilling the study's objectives. Eight of the selected factors are considered static variables and include elevation, slope, aspect, curvature, plan curvature, profile curvature, distance from major river and soil texture. The remaining six variables are dynamic and change on yearly basis. These include soil moisture, soil evaporation, land cover, precipitation and NDVI. Dust sources' locations, river data, soil texture and DEM-related inputs (elevation, slope, aspect, curvature, profile curvature and plan curvature) were provided by the Project team members.

Static variables

Soil texture

The soil texture dataset includes twelve classes: clay, silty clay, sandy clay, clay loam, silty clay loam, sandy clay loam, loam, silty loam, sandy loam, silt, loamy sand, and sand. The dataset was sourced from the *OpenLandMap* Soil Texture Class at 250 m spatial resolution, which was resampled to match the 1 km spatial resolution of the study by the Project members. The most prominent soils in the study areas are summarised in *Table 2*.

Table 2. Most prominent soil types in all study areas.

Area	***Soil 1***		***Soil 2***		***Soil 3***	
TERB	Loam	34%	Sand	21%	Sandy loam	18%
Area 1	Sandy loam	47%	Sand	23%	Loamy sand	17%
Area 2	Sand	37%	Clay loam	18%	Sandy loam	17%
Area 3	Sandy clay loam	27%	Sandy loam	22%	Clay loam	21%

Elevation, slope, aspect, curvature, profile curvature and plan curvature

The DEM was obtained from the Advanced Spaceborne Thermal Emission and Reflection Radiometer (ASTER) Global Emissivity Dataset. Other topographic factors including the slope and curvatures were generated in ArcGIS by the Project members using the DEM. The original DEM, at 100 m spatial resolution, and all topographic factors were resampled to match the 1 km spatial resolution of the study. Summary statistics for elevation and slope in all areas are presented in *Table 3*.

Table 3. Elevation and slope summary statistics.

Area	***Elevation (m)***				***Slope (°)***			
	Min	Max	Median	Std. Dev.	Min	Max	Median	Std. Dev.
TERB	0	3707	425	646	0	29.8	0.3	2.87
Area 1	151	572	241	56	0	3.54	0.2	0.25
Area 2	9	291	60	60	0	1.88	0.11	0.15
Area 3	0	187	8	31	0	0.97	0.02	0.09

Distance from rivers

The river dataset was available from HydroSHEDS (Lehner and Grill, 2013) and includes major canals and rivers characterised by high level of tributary integration. Distance from rivers raster was created in ArcGIS and covers the range from 0 to 403 km. Locally, the ranges reach 94 km in *Area 1*, 118 km in *Area 2* and 88 km in *Area 3*.

Dynamic variables

Precipitation

Monthly Global Precipitation Measurement (GPM) v6 product (Huffman et al., 2019) at 0.1° spatial resolution was acquired through the Google Earth Engine (GEE). Average annual precipitation was calculated for the time-period between 01-2001 and 12-2020. As the original monthly data was provided in mm/hr, the calculated average was multiplied by 8760 hours in a year. The resulting raster was then downscaled using the nearest neighbour interpolation to match the 1 km spatial resolution of the study. Summary statistics for 2020 for all study areas are presented in *Table 4*.

Table 4. Summary statistics for precipitation data in 2020.

Area	***2020 Precipitation (mm/year)***			
	Min	Max	Median	Std. Dev.
TERB	58	870	252	198
Area 1	131	307	182	28.6
Area 2	87	219	141	23.7
Area 3	164	485	228	60.9

Soil Moisture

The Global Surface Soil Moisture (GSSM1km) dataset was available through the GEE. This product was created by Han et al. (2023) using International Soil Moisture Network (ISMN), remote sensing and meteorological data, taking physical processes impacting soil moisture dynamics into account. This product has a 1 km spatial and daily temporal resolution and provides soil moisture data at 0-5 cm depth in cm^3/cm^3 units. Extraction and calculation of the yearly and monthly average values for the time-period between 1-01-2001 and 31-12-2020 were performed in the GEE. This dataset was masked by its authors and contains no data at set locations of water bodies. Summary statistics for 2020 for all areas are presented in *Table 5*.

Table 5. Summary statistics for soil moisture data in 2020.

Area	***2020 Soil moisture (cm^3/cm^3)***			
	Min	Max	Median	Std. Dev.
TERB	0.06	0.29	0.16	0.03
Area 1	0.12	0.22	0.15	0.01
Area 2	0.11	0.23	0.14	0.02
Area 3	0.11	0.22	0.14	0.02

Soil Evaporation

Soil evaporation data was available as part of the Penman-Monteith-Leuning Evapotranspiration V2 (PML_V2) product (Gan et al., 2018, Zhang et al., 2016, Zhang et al., 2019). The dataset was accessible from the GEE at 500 m spatial and 8-day temporal resolution in mm/day units. The calculation of average yearly data between 1-01-2001 and 31-12-2020 and its extraction was performed in the GEE. The original rasters were resampled to match the 1 km spatial resolution of the study. This dataset contains no data at the locations of water bodies. Summary statistics for 2020 for all study areas are presented in *Table 6*.

Table 6. Summary statistics for soil evaporation data in 2020.

Area	***2020 Soil evaporation (mm/day)***			
	Min	Max	Median	Std. Dev.
TERB	0	1.54	0.37	0.15
Area 1	0.08	1.31	0.4	0.06
Area 2	0.05	0.74	0.27	0.05
Area 3	0	0.92	0.32	0.08

Vegetation cover

Vegetation cover of the area is represented by the NDVI values acquired from the Modis/Terra Vegetation Indices MOD13A2.061 product (Didan K., 2021). This product was available at 1 km spatial resolution and 16-day temporal resolution. Yearly median values at pixel level for the time-period between 1-01-2001 and 31-12-2020 were extracted using the GEE. Summary statistics for 2020 for all study areas are presented in *Table 7*.

Table 7. Summary statistics for vegetation cover data in 2020.

Area	***2020 Vegetation cover (NDVI)***			
	Min	Max	Median	Std. Dev.
TERB	-0.2	0.73	0.14	0.09
Area 1	-0.01	0.43	0.11	0.04
Area 2	-0.2	0.59	0.11	0.1
Area 3	-0.2	0.69	0.12	0.1

Land cover

Annual University of Maryland (UMD) land cover classification data for 2001 to 2020 was available from the MODIS Land Cover Type Yearly Global 500m SIN Grid V061 (MCD12Q1.061) product (Friedl and Sulla-Menashe, 2022). This dataset was acquired from the GEE and was resampled to match the 1 km spatial resolution of the study. The classes were reclassified to match the objectives of the study and are presented in *Table 8*. Permanent wetlands and Cropland/Natural vegetation classes were not present in the study area. Most prominent land cover classes for each area in 2020 are presented in *Table 9*.

Table 8. Reclassification of the Annual University of Maryland land cover classification used in the study.

Original no.	***Original class name***	***Reclassified no.***	***Reclassified class name***
0	Water Bodies	0	Water bodies
1	Evergreen Needleleaf Forests	1	Natural vegetation
2	Evergreen Broadleaf Forests		
3	Deciduous Needleleaf Forests		
4	Deciduous Broadleaf Forests		
5	Mixed Forests		
6	Closed Shrublands		
7	Open Shrublands		
8	Woody Savannas		
9	Savannas		
10	Grasslands		
11	Permanent Wetlands	2	Permanent wetlands
12	Croplands	3	Croplands
13	Urban and Built-up Lands	4	Urban
14	Cropland/Natural Vegetation Mosaics	5	Cropland/Natural vegetation
15	Non-Vegetated Lands – barren lands	6	Bare ground

Table 9. Distribution of most prominent land cover classes in the TERB and in three study areas in 2020.

Area	***Class 1***		***Class 2***		***Class 3***	
TERB	Bare ground	44%	Natural vegetation	36%	Cropland	17%
Area 1	Bare ground	87%	Natural vegetation	8%	Cropland	3.5%
Area 2	Bare ground	65%	Natural vegetation	14%	Cropland	11%
Area 3	Bare ground	47%	Natural vegetation	45%	Cropland	5%

Lake size

The lake size dataset for years 2001 to 2020 was extracted from the NDVI dataset in ArcGIS Pro through reclassification of negative NDVI values that represent water pixels.

Dust storm sources

Naghibi et al. (2023) identified dust storm sources through visual interpretation of True Color Composite images from MODIS Terra/Aqua bands 1, 4 and 3. As short term dust storms were not possible to identify through MODIS imagery, the dates of longer lasting dust storms in the TERB region were obtained from a study by Boloorani et al. (2022). Non-dust sources were created by the Project members, using a random-systematic sampling method, ensuring the points were not located within a vicinity of active dust sources. The dataset with 951 dated dust source locations for 2001 to 2020 was provided by the Project members (*Figure 3*).

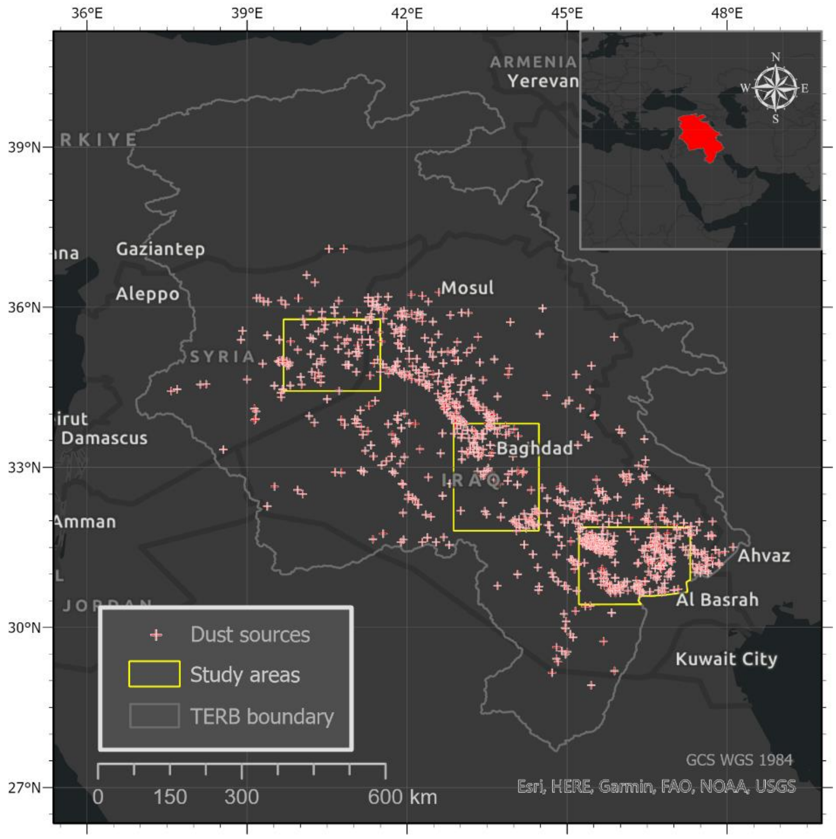

Figure 3. Distribution of dust storm sources between 2001-2020 in the TERB, with highlighted study areas.

3.1.3. Data preparation and analysis

Data exploration was performed to better understand the datasets, ascertain the quality of data and the relationships between variables. As a first step, as recommended by Guyon & Elisseeff, (2003) a correlation matrix was created for all input variables for 2020 (*Figure 4*). Initial analysis focused mainly on the dynamic factors that can be influenced by human intervention and as such formed the basis for dust storm control simulations. These factors included land cover, soil moisture, soil evaporation, NDVI and lakes. The correlation coefficients between them were explored through the analysis of the correlation matrix.

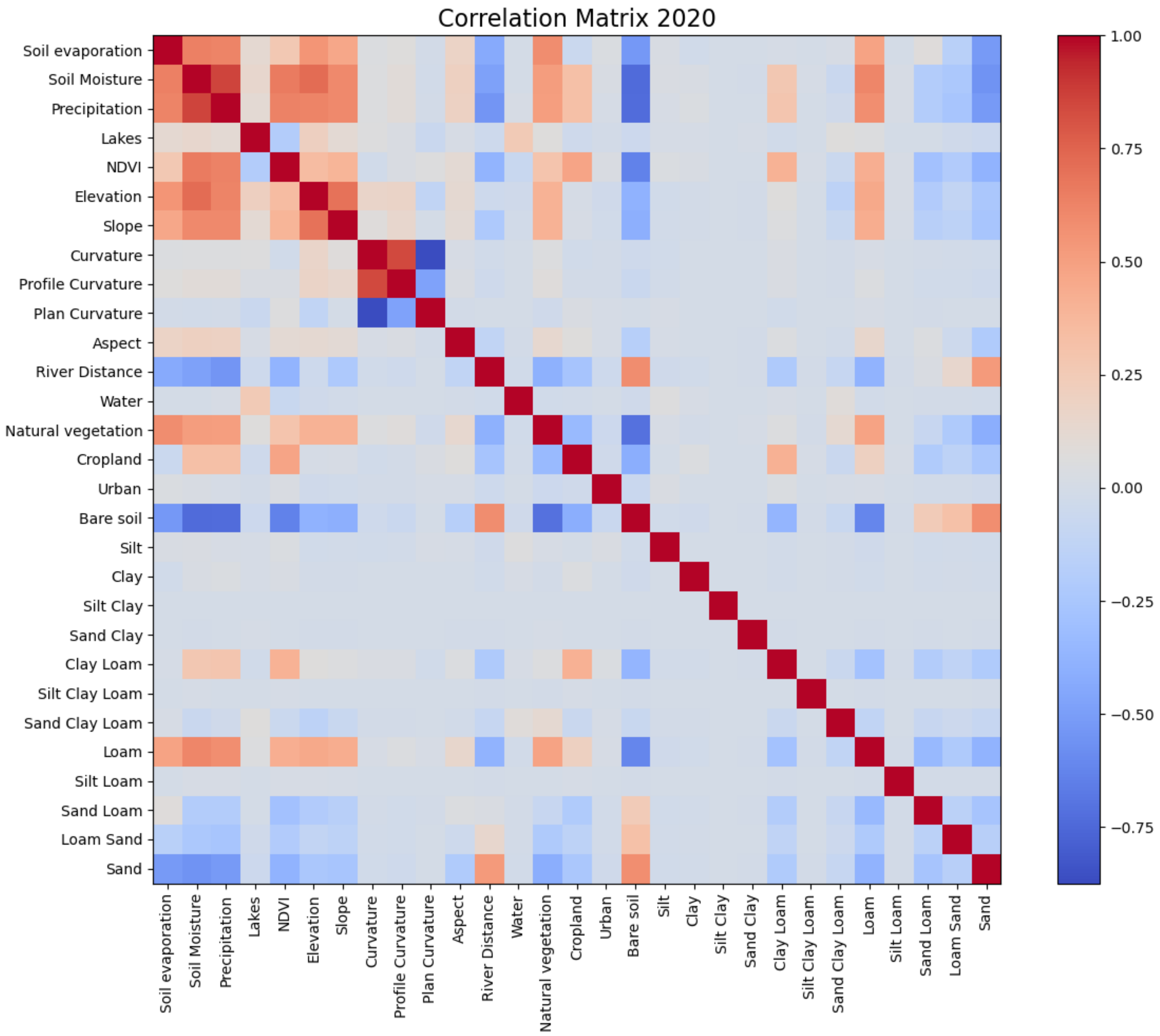

Figure 4. Correlation matrix for all XGBoost input variables for 2020.

Histograms for several driving factors at dust and non-dust source locations were created to examine the distribution and patterns of selected variables' values (*Figures 5* and *6*).

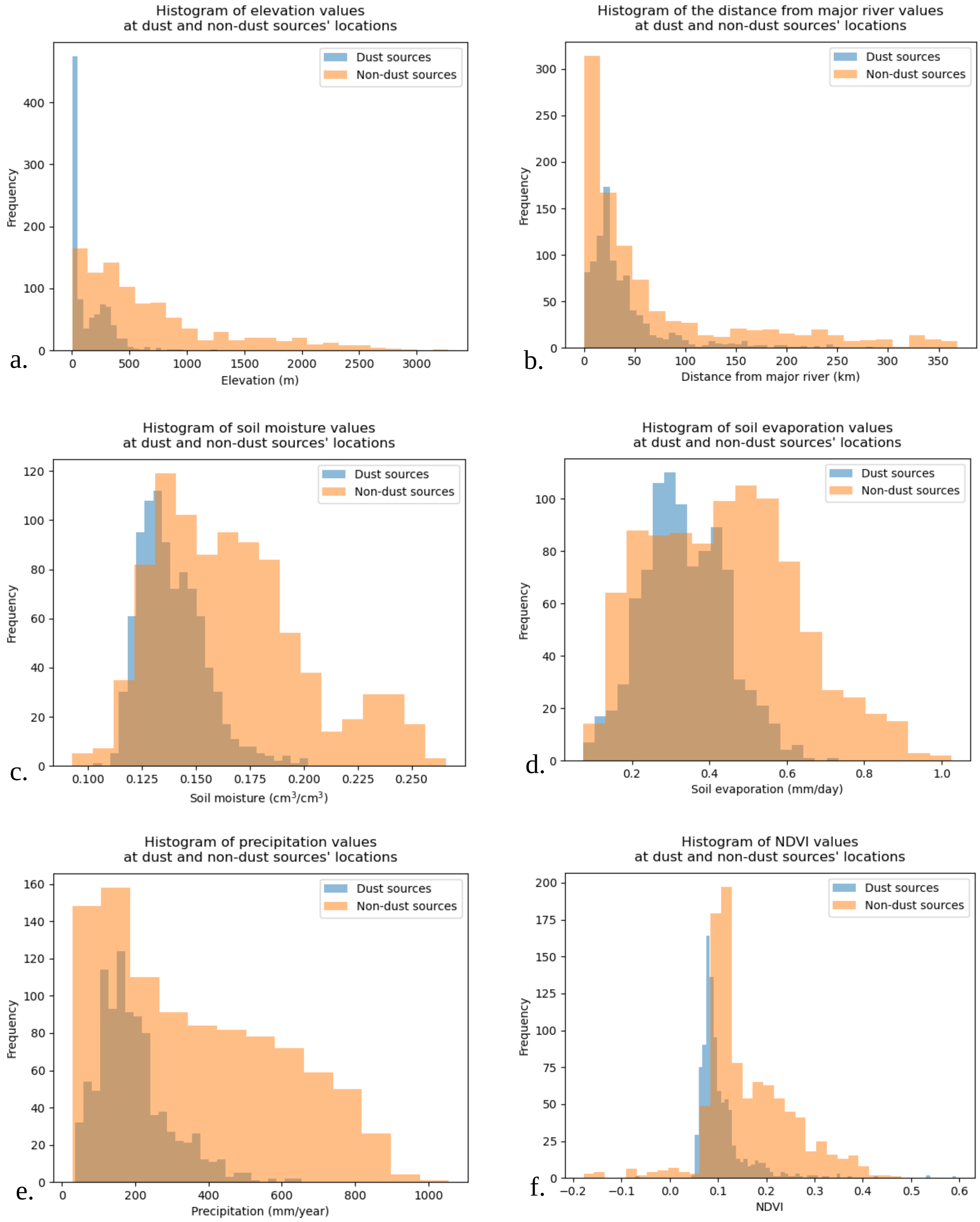

Figure 5. Histograms for values at dust and non-dust sources' locations in the TERB for a. elevation, b. distance from river, c. soil moisture, d. soil evaporation, e. precipitation and f. NDVI

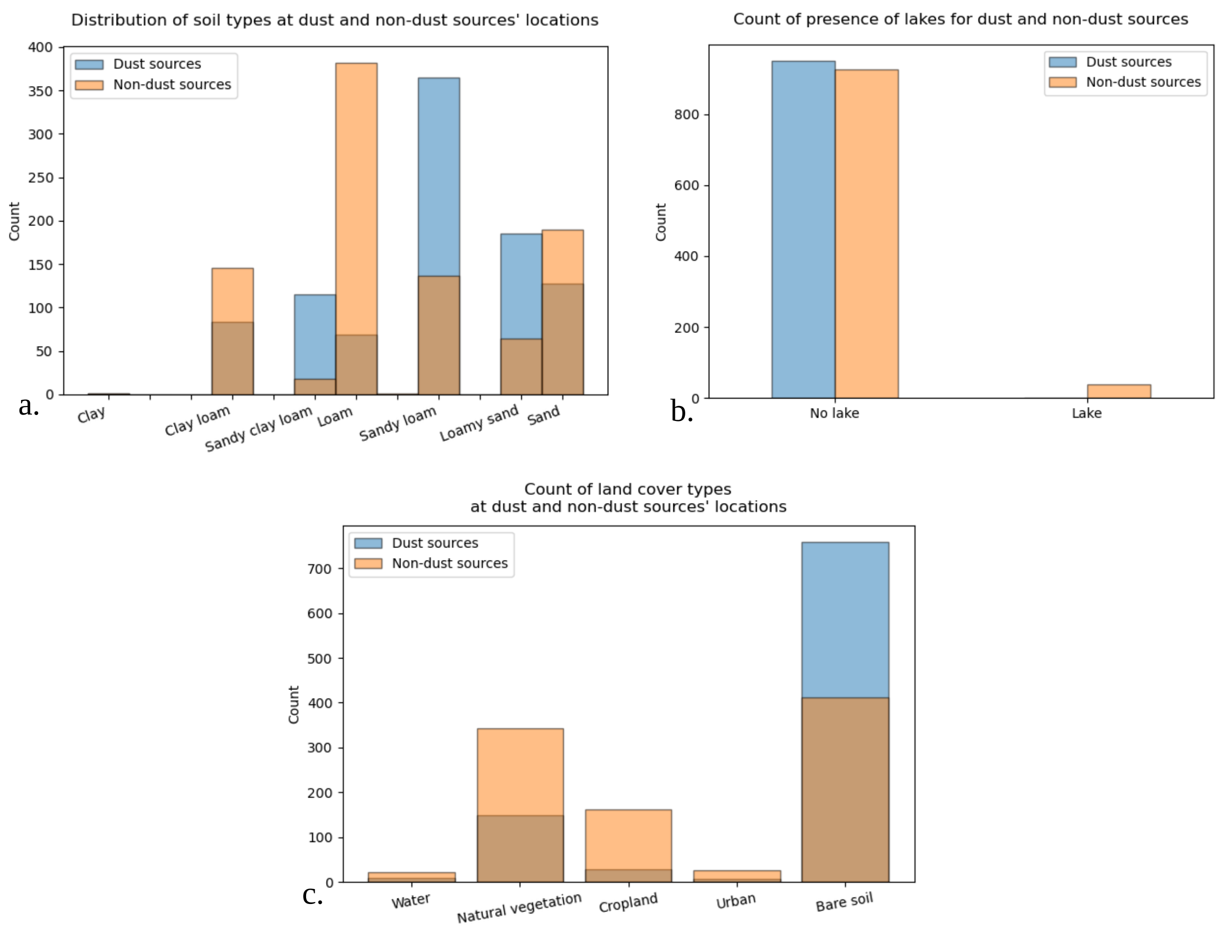

Figure 6. Distribution and count of categorical inputs at dust sources and non-dust sources location in the TERB for: a. soil type, b. presence of lakes and c. land cover types

Despite considerable overlap in some values at dust and non-dust sources, certain patterns emerged. Notably, a large proportion of dust sources were found at low elevations as shown in *Figure 5a*. Dust sources were also mostly present at NDVI values around 0.1, indicating bare soil as depicted in *Figure 5f*. This finding was further supported by the distribution of land cover classes shown in *Figure 6c*. Dust sources exhibited prominent peaks around soil moisture values of 0.13 (*Figure 5c*), and soil evaporation values of 0.3 (*Figure 5d*). Additionally, *Figures* 5c, *5d* and *5f* demonstrate that higher values of soil moisture, soil evaporation and NDVI were mostly associated with non-dust sources. Furthermore, *Figure 6c* illustrates a lower occurrence of dust sources in areas characterised by natural vegetation and cropland. These findings align with existing literature justification on dust storm and desertification mitigation strategies that involve increasing vegetation cover through forage and/or crop production (Amiraslani and Dragovich, 2011, Azoogh et al., 2018, Park et al., 2020, Maleki et al., 2021, Wang et al., 2010, Tan et al., 2015). Additional findings that reflected on the nature of dust sources include a large majority of sources appearing at distances of less than 50 km from a major river with a peak at around 20-25 km (*Figure 5b*). Non-dust sources were most prominent at close distances to a river (< 10 km), however, approximately 14% of all dust sources were recorded within the same range, which increased to 22% at 15 km. Soil type (*Figure 6a*) significantly influenced the formation of dust sources, with nearly 40% of all registered sources originating from sandy loam soils, while approximately 14% were non-dust sources. Conversely, non-dust sources were predominantly linked to loam soil texture, accounting for 40%, in contrast to only 7% of dust sources.

The alignment and harmonization of the raster datasets was meticulously performed to ensure that all pixels across the 20-year timespan corresponded precisely to the same positions in all input layers. This was done to ensure the accurate alignment required for the proper training and functioning of the XGBoost model.

Data issues

Initially, the presence of missing data posed a challenge for the soil moisture and soil evaporation datasets. Various approaches were considered to impute the missing values. However, as it was determined that the missing values primarily corresponded with the water bodies where, in the context of this study, no soil is present, it was decided to retain the missing values rather than impute them. Furthermore, it was observed that occasional inconsistencies existed between the values in these datasets and the lake dataset. To ensure alignment and coherence among the variables for the simulation purposes, a lake mask was applied changing the values to no data at the lake mask's locations.

3.2. Methodology

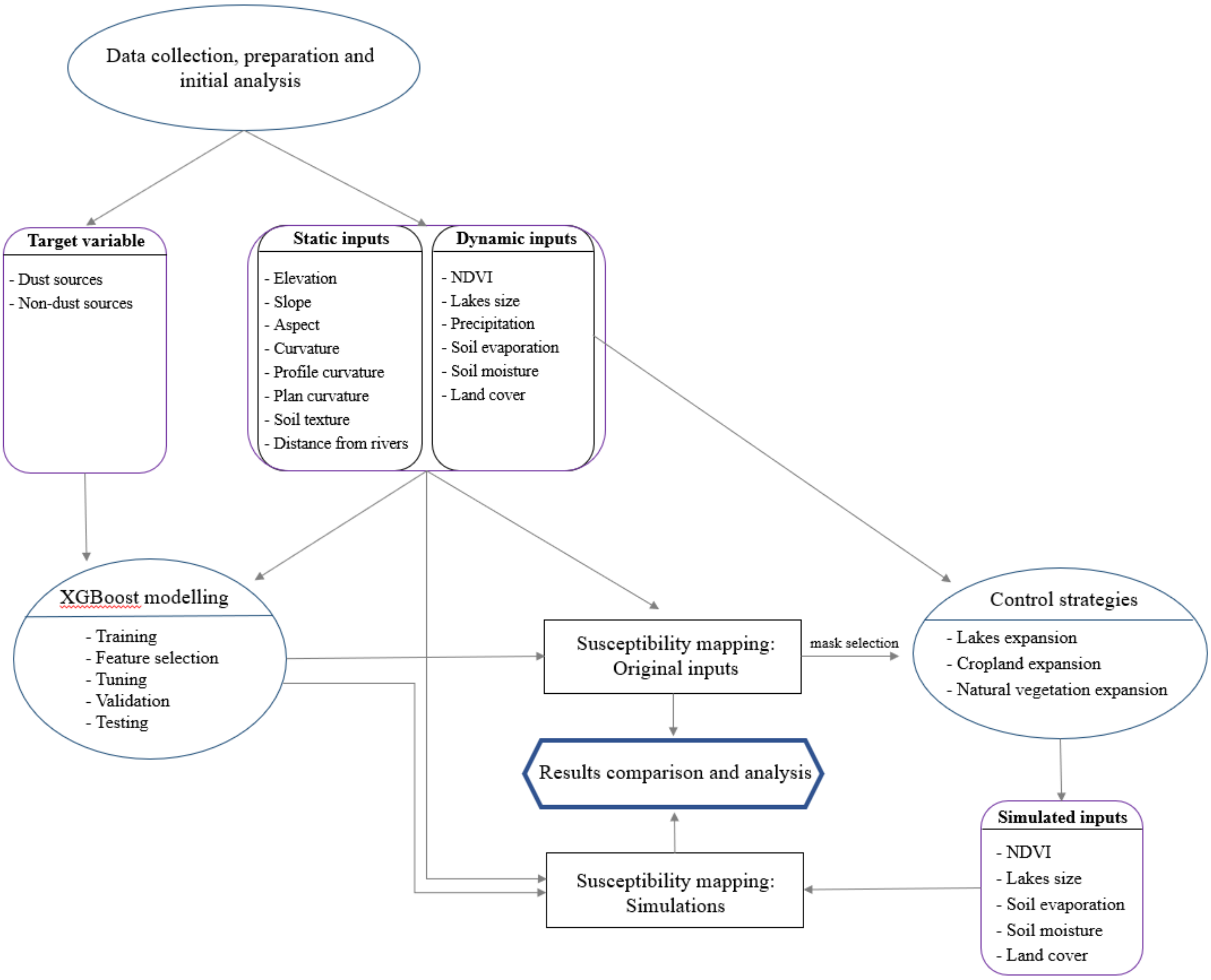

Figure 7. Flowchart representing the main stages undertaken in the study workflow.

Figure 7 presents the main stages of conducting the present research. First, all necessary data was collected, harmonized, and prepared for XGBoost modelling. Initial exploration of the data was performed to ascertain data quality, relationships, and correlation between variables. Second, using all the original inputs and the target variable, each XGBoost model was trained, tuned, validated, and tested to determine its level of performance. Next, the model was applied to the entire TERB region for 2020 and higher susceptibility regions were selected as study areas for control strategies simulations. As part of the simulations, changes were made in each relevant input layer corresponding to each study area, in accordance with the type of dust control strategy being conducted. The selection of a mask, which is a layer used to determine the areas to be affected by a particular strategy, was based on the initial susceptibility of those areas. At the final stage, the models were used to create numerous dust storm susceptibility maps, both with the original and simulated input data. These results were then compared and analysed to quantify the effects of the control strategies on the study areas and the impact of including neighbourhood effects in the machine learning model.

3.2.1. XGBoost models

To fulfil the aim of the project, a dust storm susceptibility model had to be created. Consequently, the following section addresses the second objective of the study, which involves creating two machine learning models utilizing the XGBoost algorithm.

XGBoost is a type of ensemble ML model that works by iteratively adding decision trees to the ensemble. It was introduced by Chen and Guestrin in 2016, as an extension to the concept of gradient boosting developed by Friedman (2001). Gradient boosting builds on the concept of the boosting technique that enhances the performance of each decision tree by correcting the errors of the previous trees. At each iteration, performance of the current ensemble is evaluated, and the focus is directed towards the samples that were the most difficult to classify correctly previously. XGBoost includes regularization techniques that help prevent overfitting and improve the generalization performance of the model. XGBoost handles missing data by default, using a sparsity-aware split finding technique that tries both directions in a split and finds a default direction by calculating the measurement of split improvement (Chen & Guestrin, 2016).

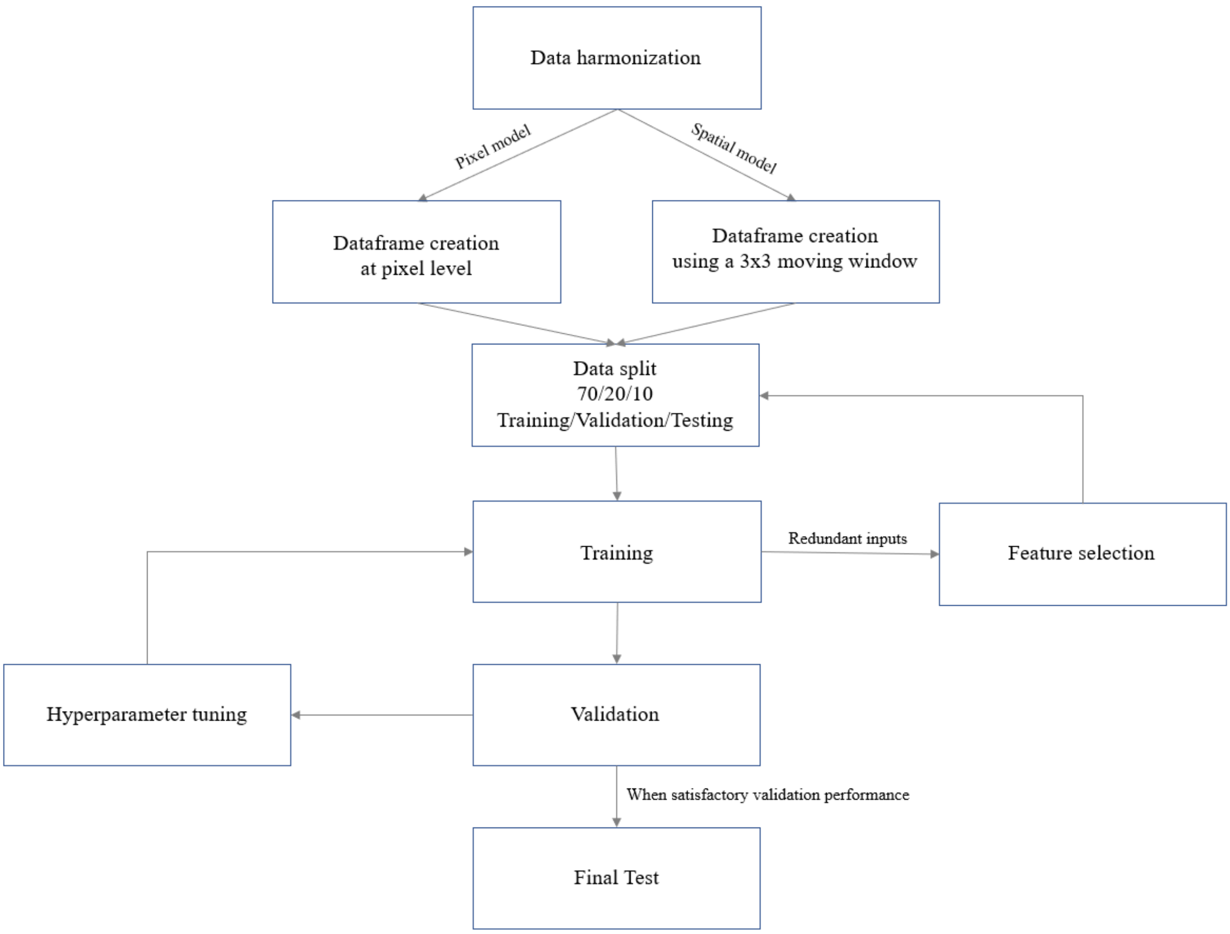

Figure 8. Flowchart showing the main stages in the XGBoost models construction.

The first step in the preparation for XGBoost training involved creating a dataframe which included all the data inputs, spanning 20 years. This dataframe collected values from every year for each input variable, encompassing both dynamic and static factors. The dynamic variables changed annually, while the static variables remained constant throughout the study period. Data was collected at the yearly locations of dust and non-dust sources, which were supplied in point feature shapefiles. The two XGBoost models created in the study adhered to a common methodology but diverged in terms of the input values incorporated into the dataframe (see *Figure 7*). The first model, referred to as the *Pixel Model* utilized pixel-level values. The second model, known as the *Spatial Model*, incorporated the spatial effect by calculating the mean value for continuous data, or the mode for categorical data, derived from the center pixel and its neighbouring pixels. As default, the moving window in the *Spatial Model* included 8 surrounding pixels (window size = 3). Any non valid pixels in the window were ignored and if no valid pixels were present in the window, the processing moved on to the next pixel location.

Once all the data was collected into the dataframe, any missing values were converted into NaNs to ensure consistency, compatibility, and data integrity. Dummy variables were created for land cover and soil texture inputs using dummy variable encoding. This encoding method involves generating a binary variable for each category, with a value of 1 where the specific category was present and 0 where it was not. This process ensures that the categorical variables are accurately represented in a numerical format suitable for modelling purposes (Brownlee, 2020). The dataframe included 30 columns and 1914 rows at this stage. *Table 10* presents a summary of all those variables. As suggested by Newman (2014), the percentage of missing values in a dataset should not exceed 10%. In the current dataset, as shown in *Table 10*, the aspect variable has a missing value percentage of 0.2%, while soil evaporation and soil moisture have missing value percentages of 1.7% and 4.4% respectively. These values are within the suggested limit.

Table 10. Summary of the initial dataframe contents for XGBoost model training.

#	*Column*	*Non-Null*	*Dtype*
0	Soil evaporation	1882	float64
1	Lakes	1914	float64
2	Precipitation	1914	float64
3	Soil moisture	1829	float64
4	NDVI	1914	float64
5	Elevation	1914	float64
6	Aspect	1911	float64
7	Curvature	1914	float64
8	Plan curvature	1914	float64
9	Profile curvature	1914	float64
10	Distance to river	1914	float64
11	Slope	1914	float64
12	Bare Soil	1914	uint8
13	Cropland	1914	uint8
14	Natural vegetation	1914	uint8
15	Urban	1914	uint8
16	Water	1914	uint8
17	Clay	1914	uint8
18	Clay loam	1914	uint8
19	Loam	1914	uint8
20	Loamy sand	1914	uint8
21	Sand	1914	uint8
22	Sandy clay loam	1914	uint8
23	Sandy loam	1914	uint8
24	Silt	1914	uint8
25	Silty loam	1914	uint8
26	Silty clay	1914	int64
27	Sandy clay	1914	int64
28	Silty clay loam	1914	int64
29	Dust source	1914	uint8

Data split

Géron (2019) suggests employing a three-way data split approach to prevent model overfitting. In this study, a split ratio of 70/20/10 was adopted, allocating 70% of the data for training (1340 points), 20% for validation (383 points), and 10% (191 points) for evaluating the final model's performance on previously unseen data. This type of division guarantees the model's generalization capability beyond the training set. A random state was set for the split, to ensure reproducibility of the randomization process and to aid in hyperparameter tuning. Once the split was established, the models were initially trained using the default parameters.

Feature selection

As explained by Friedman (2001), trees are quite robust against irrelevant input variables, however, a model can still benefit from lowering the dimensionality by removing unnecessary inputs. Within XGBoost, there are built-in functionalities that allow for assessing the importance of features using different metrics such as weight, cover, and gain (XGBoost, 2022). The weight metric refers to the number of times a feature is used to make splits in the decision trees. The cover metric represents the average coverage of a feature across all the trees in the model. It measures the relative quantity of observations associated with a particular feature. The gain metric calculates the average improvement in the model's loss function (reduction in the error) attributed to a particular feature when it is used for splitting. It reflects the usefulness of a feature in improving the model's predictive performance. *Figure 9* shows the results of in-built feature importance analysis by XGBoost.

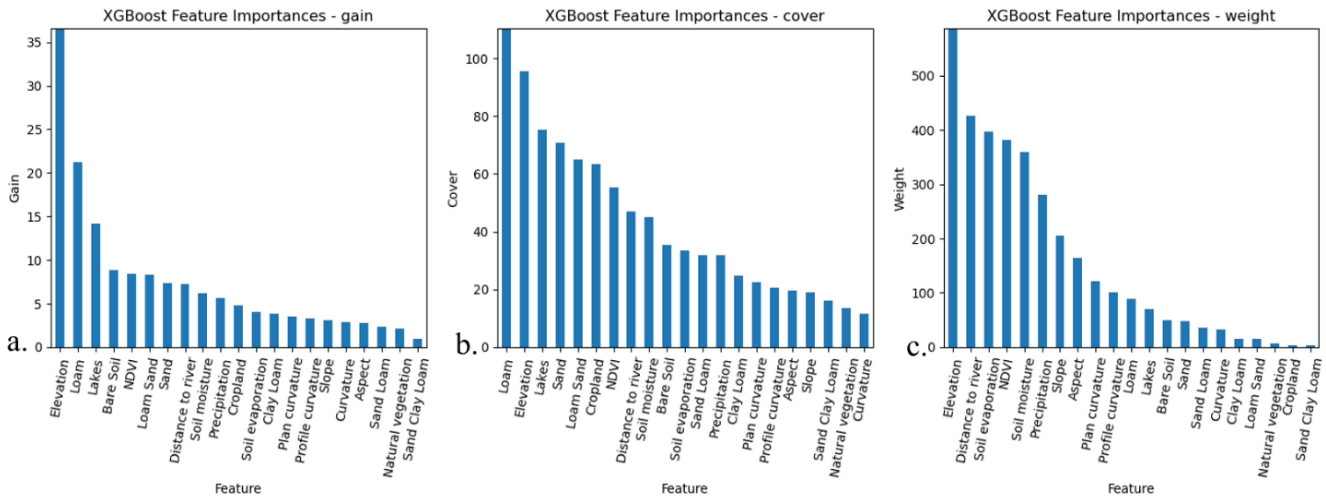

Figure 9. XGBoost built-in feature importance analysis for a. gain, b. cover and c. weight

A total of 21 features were identified to have influence on both models' performance, while the remaining 8 features were found to have no impact. These eight variables were removed from the original dataframe to decrease the number of unnecessary inputs. These variables included the water and urban land cover classes and six soil types, namely clay, silt, silty loam, silty clay, sandy clay, and silty clay loam. According to the gain metric, the three most important variables in the models are elevation, loam soil texture and lake size. Out of the dynamic factors, the most important variable was the NDVI, followed by soil moisture, precipitation and soil evaporation.

Evaluation and tuning

Previous studies on dust source susceptibility mapping emphasize the significance of incorporating validation and evaluation as integral components of the modelling process (Jafari et al.,2022, Boroughani et al., 2020, Pourhashemi et al., 2022). Validation is a process of evaluating the performance and the generalization ability of a trained model using an independent dataset (20% of the dataframe, as described in the *Data Split* section). In this study, the evaluation was used to ascertain the improvements in the models achieved through hyperparameter tuning. As used in previous studies on various susceptibility mapping problems, the performance and error metrics for the default parameters in *Pixel and Spatial Models* are presented in *Table 11*.

The confusion matrix summarizes the performance of a classification model by presenting the counts of true positive (TP), true negative (TN), false positive (FP) and false negative (FN) predictions made by the model. Accuracy metric measures the proportion of correctly classified instances out of the total number of instances in the dataset. Precision metric measures the proportion of true positive predictions out of the total predicted positives. Recall metric measures the proportion of true positive predictions out of the total actual positive instances. F1-score evaluation metric combines precision and recall into a single value. The AUC (Area Under the Curve) is a metric that summarizes the overall performance of a classification model by measuring the area under the Receiver Operating Characteristic (ROC) curve, which plots the recall against the false positive rate. As such, it shows the model's ability to distinguish between positive and negative instances (XGBoost, 2022). All the above metrics range between 0 and 1, with 1 indicating excellent performance. True Skill Statistics (TSS), as used by Jafari et al. (2022), combines recall and true negative rate into a single measure that assesses the overall performance of a classification model. TSS value ranges from -1 to 1, with 1 indicating perfect classification performance, 0 indicating random performance and negative values indicating worse-than-random. It is calculated using the confusion matrix elements as presented in *Equation 1*.

$$TSS = \frac{TP}{TP+FN} - \frac{FP}{FP+TN} \qquad \text{(Equation 1)}$$

Cross-validation is a commonly used technique for model evaluation and tuning that provides a more robust and reliable estimate of the model's performance and helps to avoid over- or underfitting. (Géron, 2019). In this study, a 5-fold cross-validation approach was employed. This means that the dataset (90% of the original dataframe) was divided into five equally sized subsets, where four subsets were used for training, and one was used for validation. This process was repeated five times, with each subset serving as the validation set once.

Table 11. Performance and error metrics for the models with default parameters settings.

	Pixel Model			Spatial Model		
Confusion matrix		*Predicted negative*	*Predicted positive*		*Predicted negative*	*Predicted positive*
	Actual negative	TN: 141	FP: 29	*Actual negative*	TN: 146	FP: 24
	Actual positive	FN: 30	TP: 145	*Actual positive*	FN: 27	TP: 148
Accuracy	82.90%			85.22%		
Precision	83.33%			86.05%		
Recall	82.86%			84.57%		
F1-score	83.09%			85.30%		
AUC	82.90%			85.23%		
TSS	0.66			0.70		
Cross-validation	85.51%, 81.45%, 81.40%, 85.17%, 81.98% Average accuracy: 83.10%			85.80%, 81.16%, 81.40%, 85.47%, 84.01% Average accuracy: 83.57%		

As can be seen from *Table 11*, the accuracies of both models were already acceptable and comparable to other ML models on susceptibility mapping (Boloorani et al., 2022, Boroughani et al., 2020, Gholami et al., 2020, Naghibi et al., 2023, Pourhashemi, 2022). According to Yesilnacar (2005), the AUC values between 0.8 and 0.9 indicate very good model performance. However, the *Spatial Model* was potentially overfitting to the training data since its cross-validation accuracy is almost 2% lower than the validation accuracy. XGBoost has over 20 hyperparameters that can be adjusted to fine-tune the model. The focus of the tuning for this study was to ensure minimal overfitting. Hyperparameters used in the tuning with their descriptions are shown in *Table 12*. To aid in the selection of hyperparameters, a RandomizedSearchCV method (Pedregosa et al., 2011) was performed on the *Pixel Model*, which randomly samples the parameter settings. A more traditionally used grid search (GridSearchCV) and specific *Spatial Model* tuning was not performed, due to time constraints.

Table 12. Hyperparameter tuning results for the Pixel Model with parameter descriptions.

Hyperparameter	***Setting***	***Parameter description***
Learning rate	0.02	Step size applied during each boosting iteration. Lower number allows for more cautious updates to the model's weights.
Max depth	5	Max depth allowed for each decision tree in the boosting process. Controls the complexity and interactions captured by trees.
Minimum child weight	2	Min sum of instance weights required in a child node for further partitioning to occur. Limits overfitting by preventing low weights.
L1, Lasso regularization	0.6	Regularization adding penalties to the weight of the leaf nodes. Encourages sparse feature weights by promoting selection of a smaller subset.
L2, Ridge regularization	0.7	Regularization adding penalties to the weight of the leaf nodes. Reduces the impact of individual features and promotes a balanced distribution of weights.
Subsample	0.7	Fraction of the training instances to be used for training. Value of < 1 introduces randomness and helps reduce overfitting.
Gamma	0.2	Specifies the minimum amount of loss reduction needed for splitting a leaf node.
Number of parallel trees	2	Determines how many tree-building rounds are performed during the training.

Using the hyperparameters shown in *Table 12,* the final training of both models was performed. The resulting performance and error metrics are presented in *Table 13*.

Table 13. Final XGBoost dust source susceptibility mapping models' performance and error metrics.

	Pixel Model			*Spatial Model*		
Confusion matrix		*Predicted negative*	*Predicted positive*		*Predicted negative*	*Predicted positive*
	Actual negative	TN: 138	FP: 32	*Actual negative*	TN: 139	FP: 31
	Actual positive	FN: 25	TP: 150	*Actual positive*	FN: 25	TP: 150
Accuracy	83.48%			83.77%		
Precision	82.42%			82.87%		
Recall	85.71%			85.71%		
F1-score	84.03%			84.27%		
AUC	83.45%			83.74%		
TSS	0.67			0.68		
Cross-validation	85.51%, 82.03%, 82.27%, 85.47%, 81.40% Average accuracy: 83.33%			85.80%, 81.45%, 83.43%, 85.47%, 81.98% Average accuracy: 83.62%		

Following the tuning, the *Pixel Model* demonstrated higher overall accuracy compared to the default settings (*Table 11*). Conversely, the *Spatial Model* showed a reduction in overfitting. The accuracy of the *Spatial Model* decreased, but the overall performance improved as it aligned with the higher accuracies obtained through cross-validation. As the final step in the evaluation, the models were evaluated on the test dataset. The results are presented in *Table 14.*

Table 14. Test evaluation metrics for the Pixel and Spatial Models.

	Pixel Model			*Spatial Model*		
Confusion matrix		*Predicted negative*	*Predicted positive*		*Predicted negative*	*Predicted positive*
	Actual negative	TN: 79	FP: 17	*Actual negative*	TN: 80	FP: 16
	Actual positive	FN: 16	TP: 80	*Actual positive*	FN: 20	TP: 76
Accuracy	82.81%			81.25%		
Precision	82.47%			82.61%		
Recall	83.33%			79.17%		
F1-score	82.90%			80.85%		
AUC	82.81%			81.25%		
TSS	0.66			0.63		

In the final evaluation, the *Pixel Model* demonstrated superior performance to the *Spatial Model* with a decrease in accuracy and AUC of less than 0.7%. The *Spatial Model* experienced a decrease in accuracy and AUC of 2.5%. Notably, the metric values for the *Spatial Model* showed reductions, indicating a potential issue of overfitting to the training data. This difference in performance can likely be attributed to the hyperparameter tuning, which was specifically conducted for the *Pixel Model* and may not have been as effective for optimizing the performance of the *Spatial Model.* Consequently, and to maintain a clear structure of the report, the *Pixel Model* was the default model used for the results presentations, apart from the analysis of the spatial effects, for which the *Spatial Model* was specifically created.

To address the fourth objective, susceptibility mapping was performed using the *Pixel* and *Spatial Models* with same dataframe structure as described in the 'XGBoost models' section. However, the selection of values for the dataframe was done on a pixel-by-pixel basis, traversing the whole input raster. This approach ensured that each pixel location in all input rasters was processed to determine its susceptibility, contributing to the overall mapping process. The initial susceptibility map was created for the TERB region using the final year's dataset (2020) with all original input variables. To facilitate a thorough analysis of the results, a 7-category labelling system was implemented. The distribution of susceptibility categories based on the model's predicted probabilities can be observed in *Table 15*. Each category (apart from the Extremely low category) encompasses a 15% difference in susceptibility. Setting smaller brackets than typically done in susceptibility mapping (usually set at 25%, such as in the study by Jafari et al. (2022) and Pourhashemi et al. (2022)), allowed for more in-depth analysis of the simulation results, which was necessary to fulfil the aim and objectives of the project.

Table 15. Susceptibility mapping categories with their corresponding probability values.

Label	***Probability***
Extremely Low	0 – 0.1
Very Low	0.1 – 0.25
Low	0.25 – 0.4
Medium	0.4 – 0.55
High	0.55 – 0.7
Very High	0.7 – 0.85
Extremely High	0.85 - 1

3.2.2. Control strategies

To address the third objective of the study, this section describes the methodologies used in the selected theoretical dust control strategies. These strategies were derived from existing literature on mitigation strategies and current regional trends, as discussed in the 'Background' section. To ensure the realism of the theoretical control strategies, three study areas were chosen based on specific criteria, including regions with high susceptibility, the presence of frequent dust sources, proximity to rivers, urban centres, and the presence of lakes. These criteria were established to meet the practical requirement of human intervention in implementing the control strategies. Selecting sites with higher susceptibility was done as part of the site selection process, which was a simplified version of the strategy presented by Maleki et al. (2021) to select sites that would benefit from the applied strategies the most.

Strategy 1 – Lake area expansion

Due to current water mismanagement issues in the region, the first simulation relates to increasing overall water inflow in *Area 2* and *Area 3*. A theoretical scenario considered for this strategy is the partial opening of the upstream dams, allowing for more water flow downstream Euphrates and Tigris. This has the potential to increase the area of water bodies in *Area 2* and *Area 3*, as the lakes there are fed by the affected rivers.

The methodology involved several steps (*Figure 10*). Firstly, a mask was created to identify additional lake pixels, randomly distributed around the existing lake area pixels, amounting to a 20% increase in the lake's overall area. This mask determined the areas where the lake expansion would occur, and land cover class would change. Next, the NDVI values at the masked locations were set to -0.1. This value was chosen as negative NDVI values represent water values, and the minimum NDVI values observed in the dataset reached -0.2. The values of soil moisture and soil evaporation at the expanded lake locations were changed to ‘NaN’ to reflect the typical conditions observed at the existing lake sites in the dataset. Finally, five new rasters (land cover, soil moisture, soil evaporation, lake size and NDVI) were saved and used in susceptibility mapping for Simulation 1.

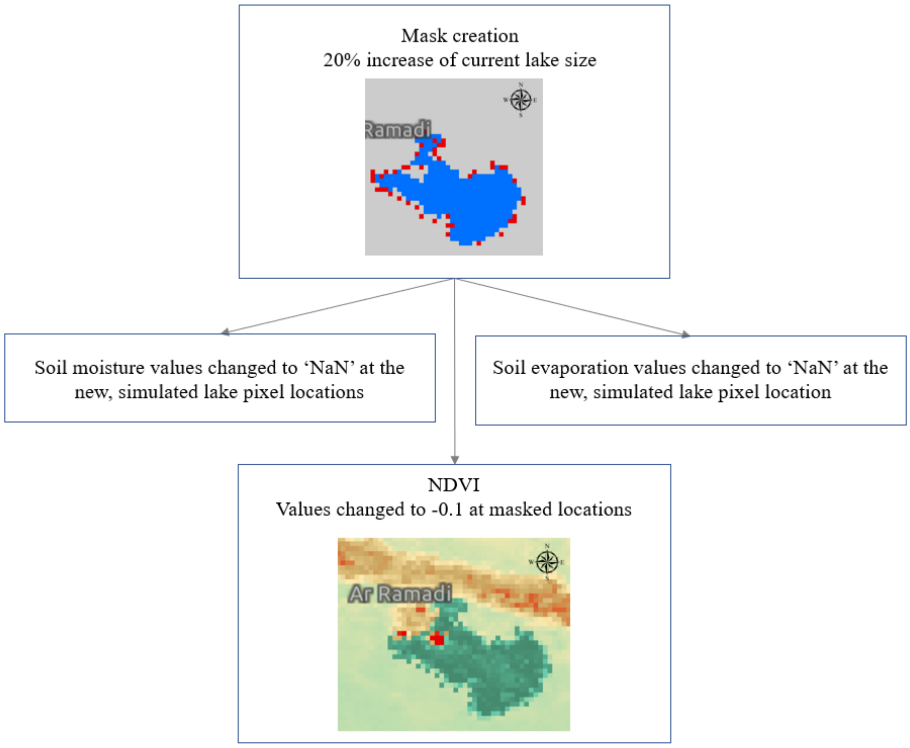

Figure 10. Flowchart showing the lake expansion simulation methodology.

Strategy 2 and Strategy 3 – Land use change

As mentioned in the 'Background' and 'Data' section, commonly undertaken dust storm mitigation strategies involve increasing vegetation cover through forage and/or crop production. Consequently, Strategy 2 involves the expansion of cropland and Strategy 3 involves the expansion of natural vegetation in bare soil regions.

To ensure a realistic approach to the LUC strategies, a conservative mask selection method was chosen. Analysis of the original susceptibility map of the TERB area revealed the presence of lower susceptibility areas within a 5 km distance from major rivers. A comparison with the land cover classes indicated that cropland and natural vegetation likely played a significant role in this finding (see example in *Figure 11*). Further examination showed a visible increase in susceptibility between 5 and 10 km, although natural vegetation occasionally extended into this range. Additionally, in the 'Data preparation and analysis' section, it was found that 14% of all dust sources in the dataset were located within the 10 km range of the rivers, with 9% being present within the 5 km range.

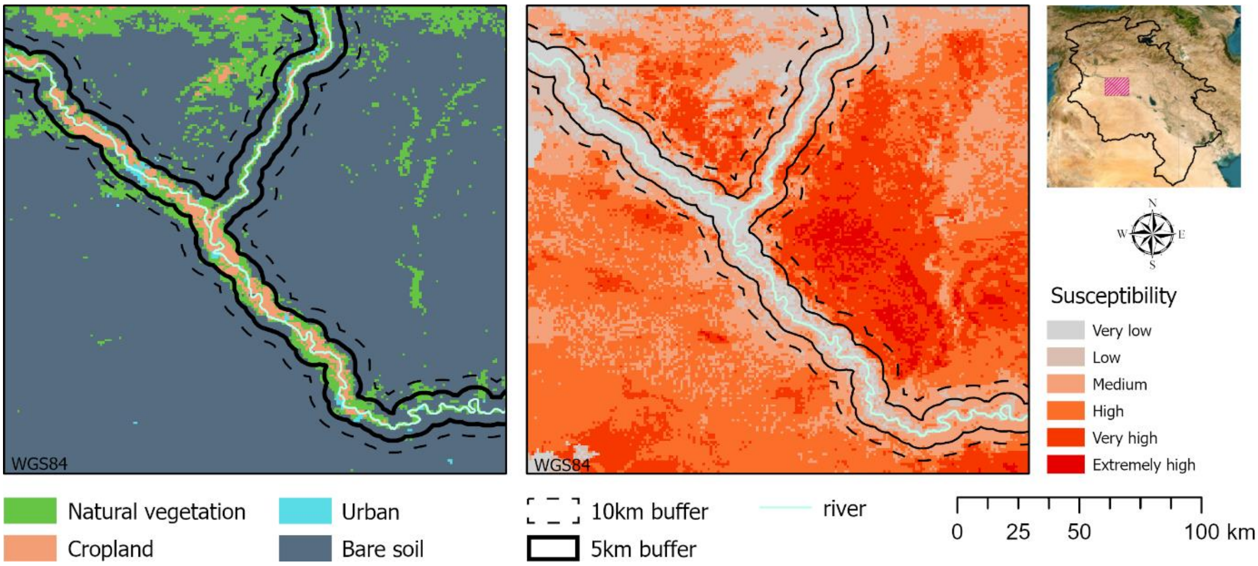

Figure 11. Land cover and susceptibility map comparison in Area 1, showing 5 km and 10 km buffer zones around the river.

Based on the above findings, a 5 km river buffer was chosen for expanding cropland cover, while a 5–10 km river buffer was selected for increasing the natural vegetation cover. The selection of a 5 km river buffer for expanding cropland cover was based on the feasibility of establishing cropland closer to the river, taking advantage of easy water access. On the other hand, the choice of a 5-10 km river buffer for increasing natural vegetation cover was driven by the understanding that natural vegetation may have better prospects further away from the river, where water access for agriculture becomes more challenging. Focusing on an area that comprises 14% of the total dust sources and implementing strategies that are relatively easier to accomplish was deemed a favourable approach. An arbitrary 20% random change in bare soil class within the river buffer was selected for each strategy. To ensure consistency and alignment between the analysis and simulation, only medium to extremely high initially susceptible areas were considered in the creation of the mask. This approach was deemed appropriate and logical considering the objectives of the study.

Both LUC strategies have similar methodologies (*Figure 12*) that differ only in the locations of the mask creations and in the applied value changes to the soil moisture, soil evaporation and NDVI layers. As finding precise data in literature to account for these values' changes between land cover classes was unsuccessful, a statistical analysis of the dataset was performed. At first, the values for NDVI, soil moisture and soil evaporation were extracted at bare soil, cropland, and natural vegetation locations, across the TERB area, throughout the 20- year study period. However, these values appeared exaggerated and consequently further analysis was performed, accounting for differences in regions and soil textures. All the results from the regional statistical analysis, with values for each land cover change at top six soil types, are presented in Appendix 1. As a result of this analysis, cropland expansion was only applied to the soils that had cropland land use classes. Consequently, no bare soil classes coinciding with sand and loam sand soil textures were affected, as cropland land use class does not coincide with these soils in the study areas. Finally, four new rasters (land cover, soil moisture, soil evaporation and NDVI) were saved for each strategy and used in susceptibility mapping for Simulation 2 and Simulation 3.

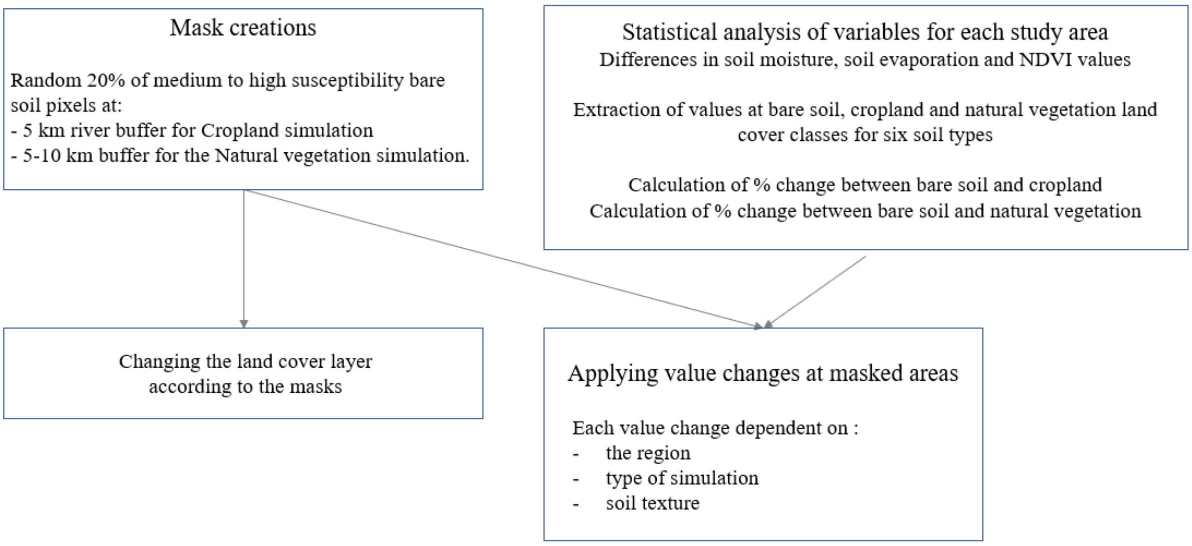

Figure 12. Flowchart showing steps undertaken in simulation 2 (cropland) and simulation 3 (natural vegetation)

Strategy 4 and Strategy 5 – Combinations

Two additional strategies tested included combining LUC strategies together in Strategy 4, and Lake expansion with both LUC strategies in Strategy 5. Both strategies inherit the same assumptions and limitations as the original simulations. As there was no mask overlap in Strategy 4, the order of applying the changes to the values at masked locations was not important. However, Strategy 5 applied Lake expansion changes to the layers first, before adjusting the values based on the LUC simulations.

3.2.3. Evaluation metrics

To address the fifth objective of the study, this research aimed to provide comprehensive and interpretable results regarding the local and regional effects of the simulations. Statistical analysis focused on two key aspects: the local effect, which examined specific areas of interest using designated buffers, and the regional effect, which involved calculations across entire study areas. This was done by comparing the original susceptibility mapping results with the simulated susceptibility mapping results. Visually, the comparison was made calculating the differences between the original and simulated rasters at pixel level. This approach was built on a commonly used approach in remote sensing, such as in Yokoya et al.'s (2022) research into landslide mapping, where the pre-disaster and post-disaster images were compared and results extracted as a separate mask. In the current study, the results show how the classification changed at each affected pixel location, by showing the number of dropped classes. For example, a drop from Extremely High to Medium susceptibility was recorded as a three classes drop.

To investigate the impacts of different LUC simulations, specific buffers were applied. A 0-5 km buffer from the river was used to analyse the effects of cropland expansion, while a buffer of 5-10 km was utilized to assess the impacts of natural vegetation expansion. Additionally, a buffer of 0-10 km was created which addressed the combined LUCs simulation (Strategy 4). A 5 km buffer was created around the original lake area to evaluate the influence of the lake increase simulation in the vicinity of the lakes. These approaches enabled a thorough examination of both the localized and broader regional susceptibility implications of the implemented strategies. In both contexts, the assessment of improvement was quantified by evaluating the percentage decrease in average susceptibility relative to the original state. Additionally, the analysis considered the disparity in the percentage distribution of Very low to Medium (Low-Med) classes and the High to Extremely high classes (High+). This was done to check how much of the highly susceptible areas fell into the lower susceptibility's brackets. Comparison of the percentage distribution of classes is commonly performed in change analysis in remote sensing studies, such as in the research by Bakr and Afifi (2019) which focused on quantifying land cover change over time.

Additionally, to determine the overall effectiveness of the simulation, a second type of metric was introduced, called the intensity of change (IOC). This metric takes both the percentage change and the percentage of the affected area into consideration and is calculated as in *Equation 2*. It was created by the author for the comparison purposes of this thesis, due to the apparent lack of similar analysis in the scientific literature.

$$IOC = \frac{original\ metric - simulated\ metric}{original\ metric} * \frac{mask\ area}{total\ area} * 100\% \qquad \text{(Equation 2)}$$

To address the spatial effect on simulations when using the *Spatial Model*, a visual interpretation of the results was performed. The process included checking if any areas in the vicinity of the applied masks have changed, by blocking out the masked pixel values and noting any differences in the surrounding pixels.

4. Results

The ‘Results’ section begins by briefly presenting the original *Pixel Model* susceptibility maps for the whole TERB area (*Figure 13*) and for each study area before any control strategies were applied (*Figures 14-16*). The section then presents the *Pixel Model* results of the simulations in each area using the relative improvement metric, showing all the main findings and the *Spatial Model’s* effect on the neighbouring pixels. Finally, the effectiveness’s of all the simulations are compared using the intensity of change (IOC) metric at the local and regional scale.

4.1. Original susceptibility maps

TERB

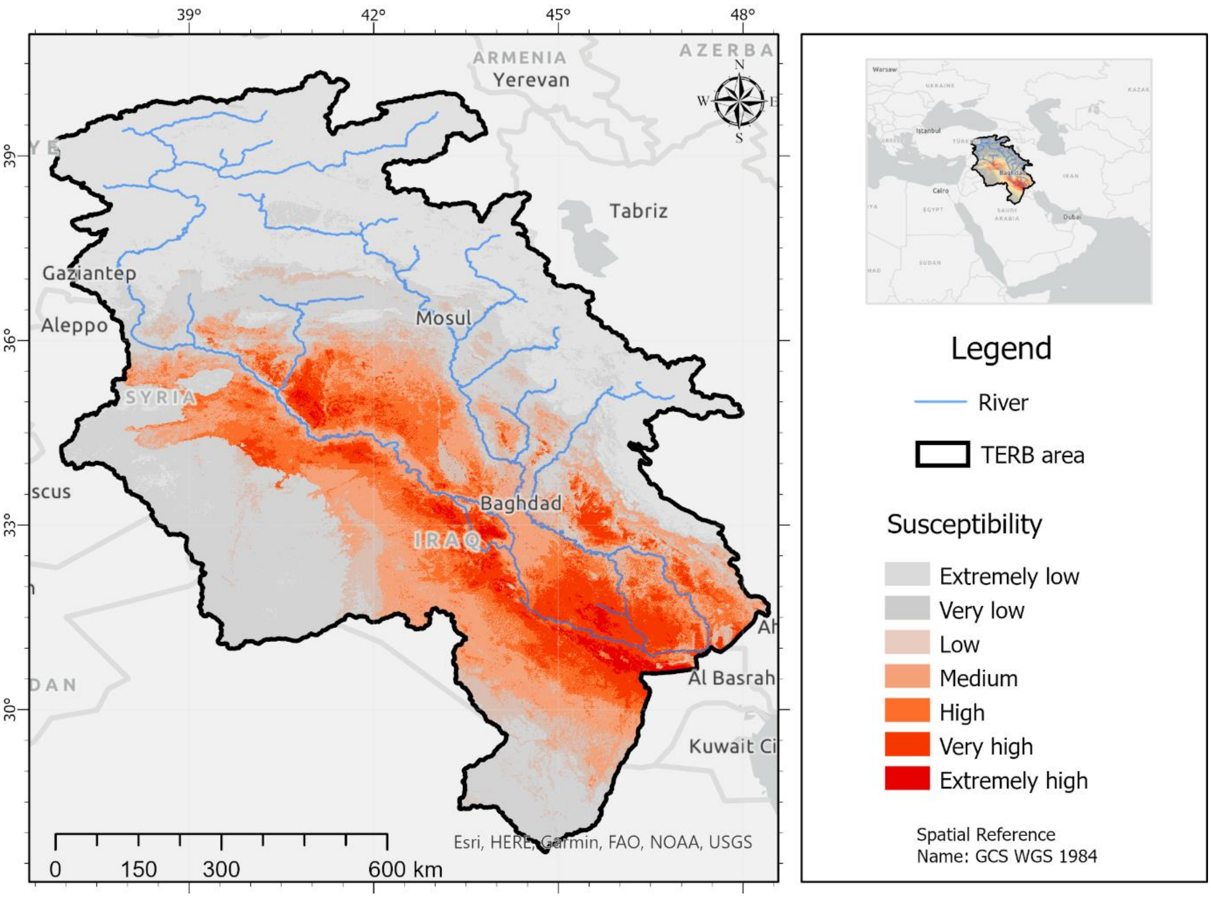

Figure 13. Initial susceptibility map for the TERB area in 2020 (Pixel Model).

The susceptibility map shows that the highest susceptibility to forming dust storms in 2020 was located in the flat, south-eastern region of the TERB associated with the marshlands. The lowest susceptibility (at probabilities of less than 10%) is present in the northern TERB, within the mountainous region. There were a number of hot spots, specifically east of Euphrates River at the Syrian-Iraq border and west of Euphrates River in central TERB. Generally, in the central and southern regions, the susceptibility is lower at water locations. While it is lower within around 5 km from the river, the susceptibility strongly increases further away and decreases again at distances greater than 100 km.

Area 1

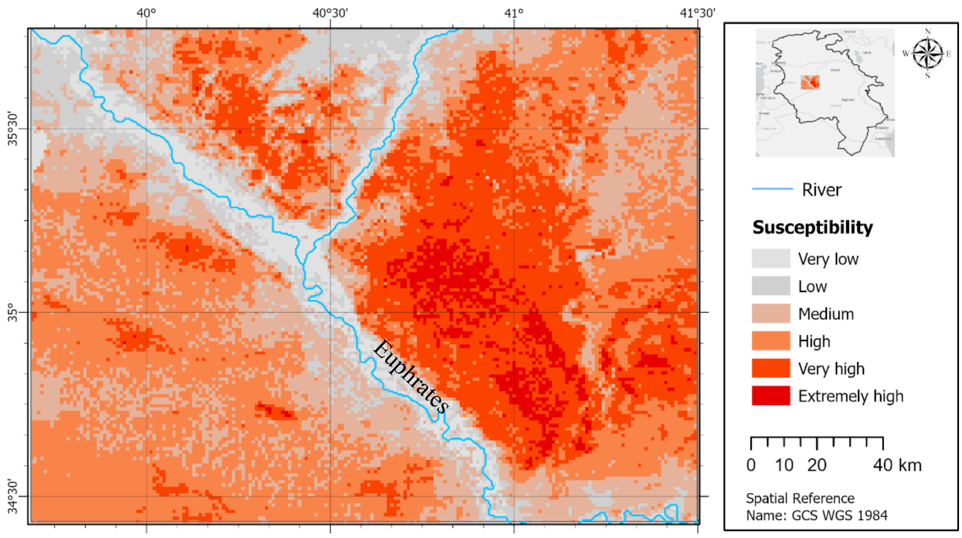

Figure 14. Initial dust source susceptibility map for Area 1 in 2020 (Pixel Model)

Average susceptibility classification in *Area 1* was 0.579, which is in the lower end of the High susceptibility category. There was a clear relationship visible between low susceptibility in the proximity of rivers (*Figure 14*). A Very High-Extremely High hot spot is present within 20-80 km north-east from the Euphrates River.

Area 2

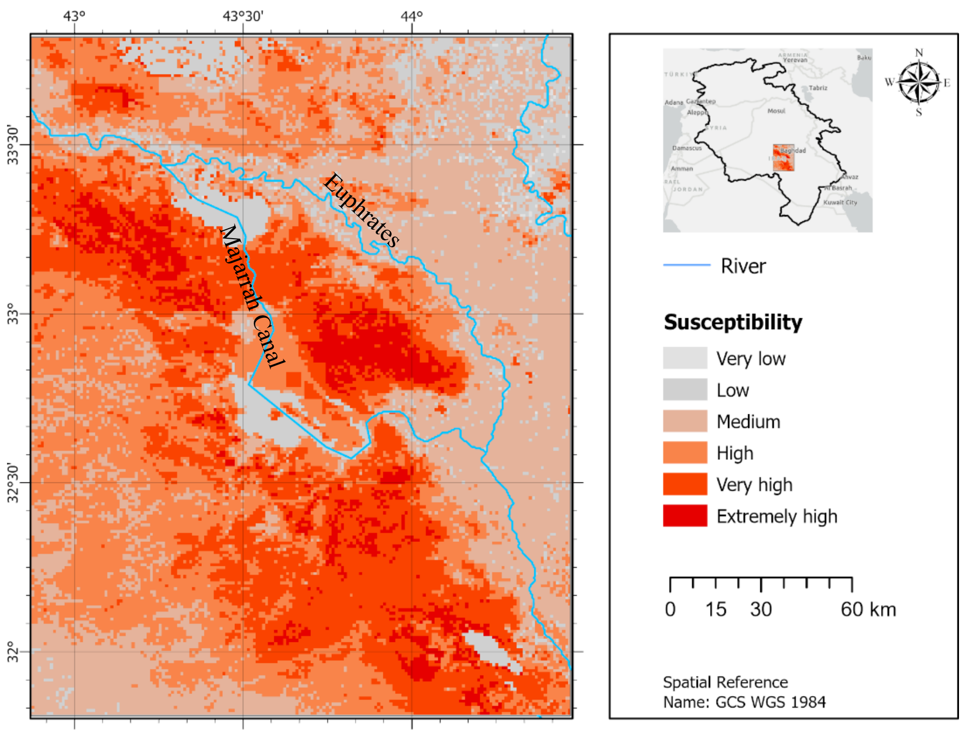

Figure 15. Initial dust source susceptibility map for Area 2 in 2020 (Pixel Model)

Average susceptibility classification in *Area 2* was 0.593, placing it in the low-mid range of the High susceptibility category. Low susceptibility classes are clearly visible at the locations of water bodies, while high susceptibility is present to the west of the Euphrates River (see *Figure*

15). The highest susceptibility area is located between the Euphrates River and the Majarrah Canal. Lower susceptibility was associated with the proximity to Euphrates River, but not with the proximity to Majarrah Canal. Lowest susceptibility is found east of the Euphrates River.

Area 3

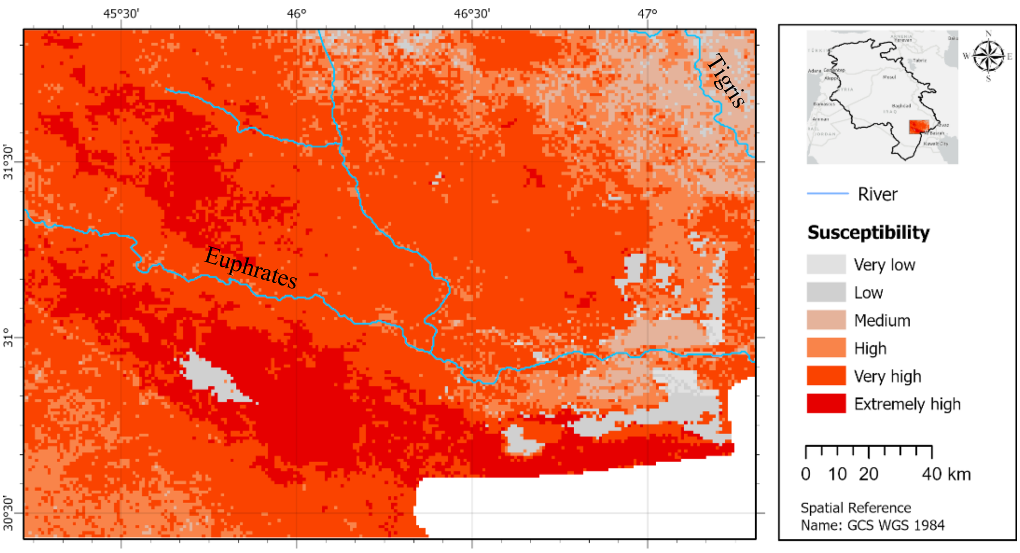

Figure 16. Initial dust source susceptibility map for Area 3 in 2020 (Pixel Model)

Average susceptibility classification in *Area 3* was 0.739. This means that the average susceptibility in the region falls within the Very High category. There is little to no association of low susceptibilities to river proximity. Lower classes of susceptibility are only present at the locations of water bodies (*Figure 16*). Additionally, the lower susceptibilities were also found within 20 km of the Tigris River in the north-east. Highest susceptibility was found around the lakes and marshlands.

4.2. Simulations results

The impact of the simulations on the regions' susceptibility to dust storms was difficult to ascertain by visual comparison of the maps alone. Consequently, the effect was presented through measuring classification differences at pixel values, portraying the original susceptibility maps together with the maps showing the difference in classification of individual pixels after the simulations. To complement the visual comparison, local and regional improvement metrics were calculated for all the simulations to assess their effectiveness.

Area 1

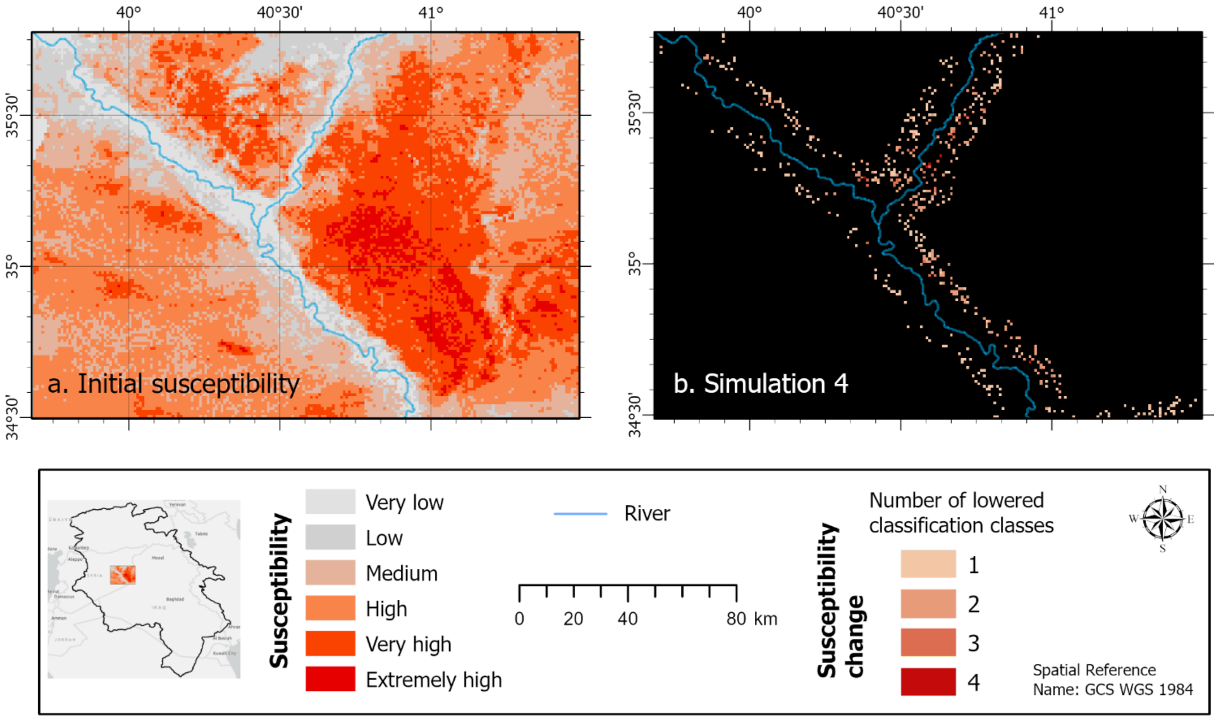

Figure 17. Spatial analysis results for susceptibility change for Area 1: a. initial susceptibility map of the area in 2020, b. susceptibility class changes following the Combined Land Use Change, Simulation 4

Figure 17 shows the visual representation of the combined LUCs simulation that accounts for the expansion of cropland at 0-5 km and natural vegetation at 5-10 km from the river. The most significant improvement in the classification is visible to the east of Euphrates River, specifically along the Al Khabour River, where a 3-4 class drop hot spot is visible. Since each category encompasses a 15% change, a 4 class drop indicates a minimum 46% decrease in the pixel's susceptibility score.

Area 1 - local effect

Table 16. Relative local effectiveness statistics for Area 1 simulations 2, 3 and 4.

Susceptibility Map	*Mask name*	*Mask area (km²)*	*Buffer area (km²)*	*Affected*	*Mean susc.*	*Mean improv.*	*High+ classes*	*Classif. Improv.*	*Neighbour effect (Spatial Model)*
Original	Cropland	175	4133	4.23%	0.331		6.99%		
Simulation 2					0.319	3.43%	5.52%	1.48%	No
Original	Natural vegetation	502	3480	14.43%	0.498		31.06%		
Simulation 3					0.474	4.76%	25.29%	5.78%	No
Original	Cropland + vegetation	677	7613	8.89%	0.407		18%		
Simulation 4					0.390	4.17%	14.55%	3.44%	No

On the local scale, the most effective simulation was the Natural Vegetation LUC with a mean improvement of 4.76% and a 5.78% drop in the High+ classes. Following a visual test, it was concluded that there was no influence of the *Spatial Model* on the pixels surrounding the masked areas.

Area 1 - regional effect

Table 17. Relative regional effectiveness statistics for Area 1 simulations.

Susceptibility Map	***Mask area (km^2)***	***Total area (km^2)***	***Affected***	***Mean susc.***	***Mean improv.***	***High+ classes***	***Classif. Improv.***
Original	-	30300	-	0.579		62.18%	
Simulation 2	175		0.58%	0.577	0.27%	61.98%	0.20%
Simulation 3	502		1.66%	0.576	0.47%	61.52%	0.66%
Simulation 4	677		2.23%	0.575	0.74%	61.32%	0.86%

On the regional scale, the largest improvement (albeit small) was achieved through the combined Cropland and Natural Vegetation LUC simulations (Simulation 4). The expansion of cropland (Simulation 2) had the smallest effect on the overall susceptibility of the area. It is worth noting, that the average regional susceptibility in the area is on average one classification class higher than the local values. Despite this, targeting the lower susceptibility areas improved the overall susceptibility by reducing the amount of higher susceptibility areas. It is worth noting the Simulation 4 appears to simply compound the effectiveness of Simulation 2 and Simulation 3.

Area 2

Figure 18 presents the original susceptibility map juxtaposed with the simulations results for *Area 2*. The Lake Expansion simulation (Simulation 1) in *Figure 18b* shows the strongest effect of a 4 class drop around the southern lake. The Combined LUC (Simulation 3) simulation in *Figure 18c* exhibits a 1 to 3 class drop, but has an extensive influence throughout the mask, except for the areas in the vicinity of Lake Razazza. The results also show that Medium susceptibility pixels have not shown significant changes in the classification at the masked area (compare *Figure 18a* with *Figure 18c* on the east bank of Euphrates River).

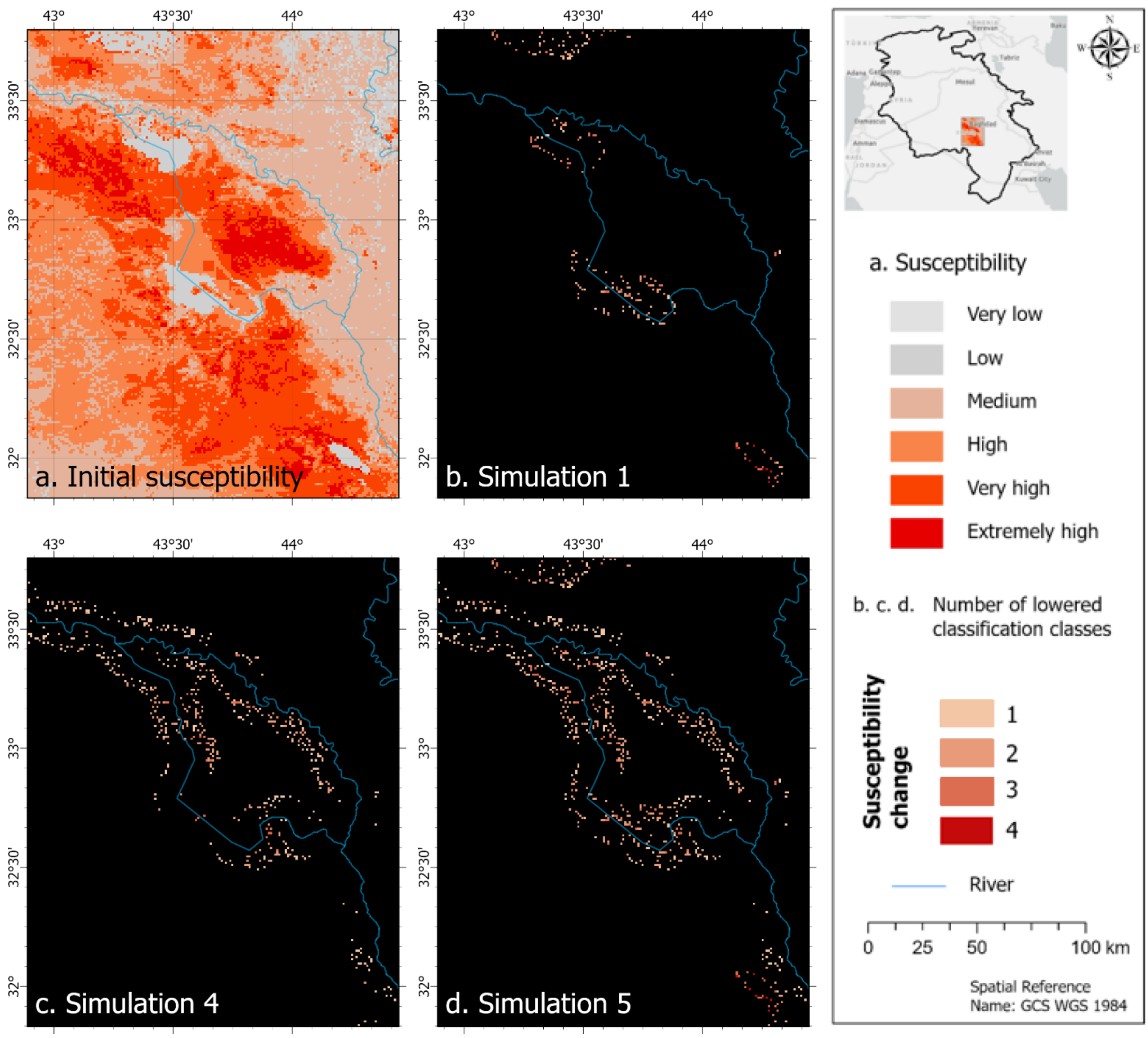

Figure 18. Spatial analysis results for susceptibility change for Area 2: a. the initial susceptibility map in 2020, b. susceptibility class changes following the Lake Expansion Simulation 1, c. susceptibility class changes following the Combined Land Use Change Simulation 4 and d. susceptibility class changes following combined Lake Expansion and Land Use Changes Simulation 5.

Area 2 - local effect

Table 18. Relative local effectiveness statistics for Area 2 simulations 1 to 5.

Susceptibility Map	*Mask name*	*Mask area (km^2)*	*Buffer area (km^2)*	*Affected*	*Mean susc.*	*Mean improv.*	*High+ classes*	*Classif. Improv.*	*Neighbour effect (Spatial Model)*
Original	Lakes	265	3002	8.83%	0.643		74.32%		
Simulation 1					0.618	3.85%	68.25%	6.06%	No
Original	Cropland	168	6903	2.43%	0.481		25.32%		
Simulation 2					0.476	1.03%	24.32%	1.36%	No
Original	Natural vegetation	494	5691	8.68%	0.560		48.88%		
Simulation 3					0.543	3.03%	42.87%	6.01%	No
Original	Cropland + vegetation	662	12594	5.26%	0.517		36.17%		
Simulation 4					0.506	2.01%	32.71%	3.46%	No
Original	Lakes + LUC	1127	13857	8.13%	0.530		39.86%		
Simulation 5					0.515	2.77%	35.46%	4.41%	No

On the local scale, the most influential simulation was the lakes expansion strategy (Simulation 1) with the highest mean and classification improvement, followed by the natural vegetation LUC strategy, Simulation 3 (*Table 18*). The smallest improvement was noted in the cropland Simulation 2, with only around 1% decrease in the average susceptibility and High+ classes. *Figure 19* shows an example result of the *Spatial Model* neighbourhood effect test. The test used the expanded lake mask to look for any classification changes outside of the masked area. As can be seen through visual comparison of the maps, there is no difference in the classification results, even when single pixels are surrounded by the mask. This result was the same across all the simulations in all areas.

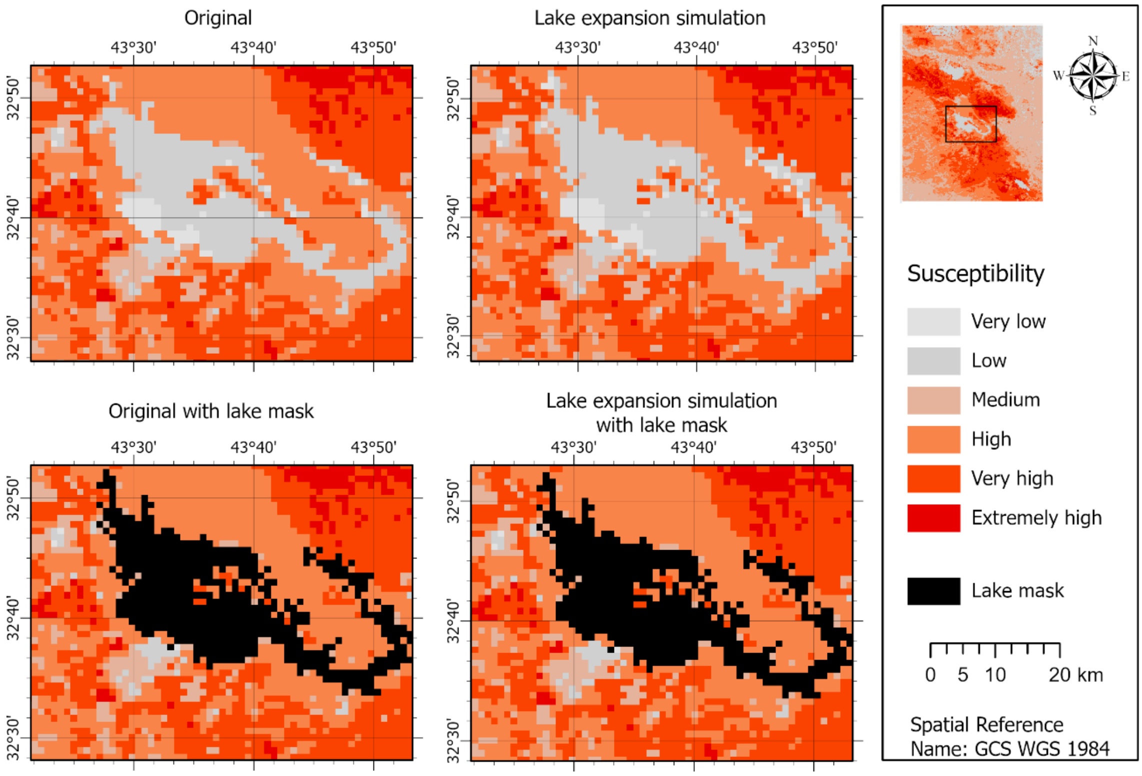

Figure 19. Example of a Spatial Model test to assess the influence of spatial effect on the neighbouring pixels. Original susceptibility map and lake expansion simulation map are shown, both with and without the lake mask used in the simulation.

Area 2 - regional effect

Table 19. Relative regional effectiveness statistics for Area 2 simulations.

Susceptibility Map	***Mask area (km^2)***	***Total area (km^2)***	***Affected***	***Mean susc.***	***Mean improv.***	***High+ classes***	***Classif. Improv.***
Original	-	39694	-	0.593		58.55%	
Simulation 1	265		0.67%	0.591	0.35%	58.04%	0.51%
Simulation 2	168		0.42%	0.592	0.15%	58.31%	0.24%
Simulation 3	494		1.24%	0.591	0.41%	57.69%	0.86%
Simulation 4	662		1.67%	0.589	0.56%	57.45%	1.10%
Simulation 5	1127		2.84%	0.587	0.90%	56.96%	1.59%

On the regional scale, the largest improvement was achieved through the combined lake and LUC, Simulation 5. The expansion of cropland (Simulation 2) had the smallest effect on the overall susceptibility. It is worth noting that the average susceptibility of the 5 km lake buffer was significantly higher than the regional susceptibility. Additionally, an observation can be made that Simulation 4 appears to simply compound the improvements from Simulation 2 and Simulation 3 together.

Area 3

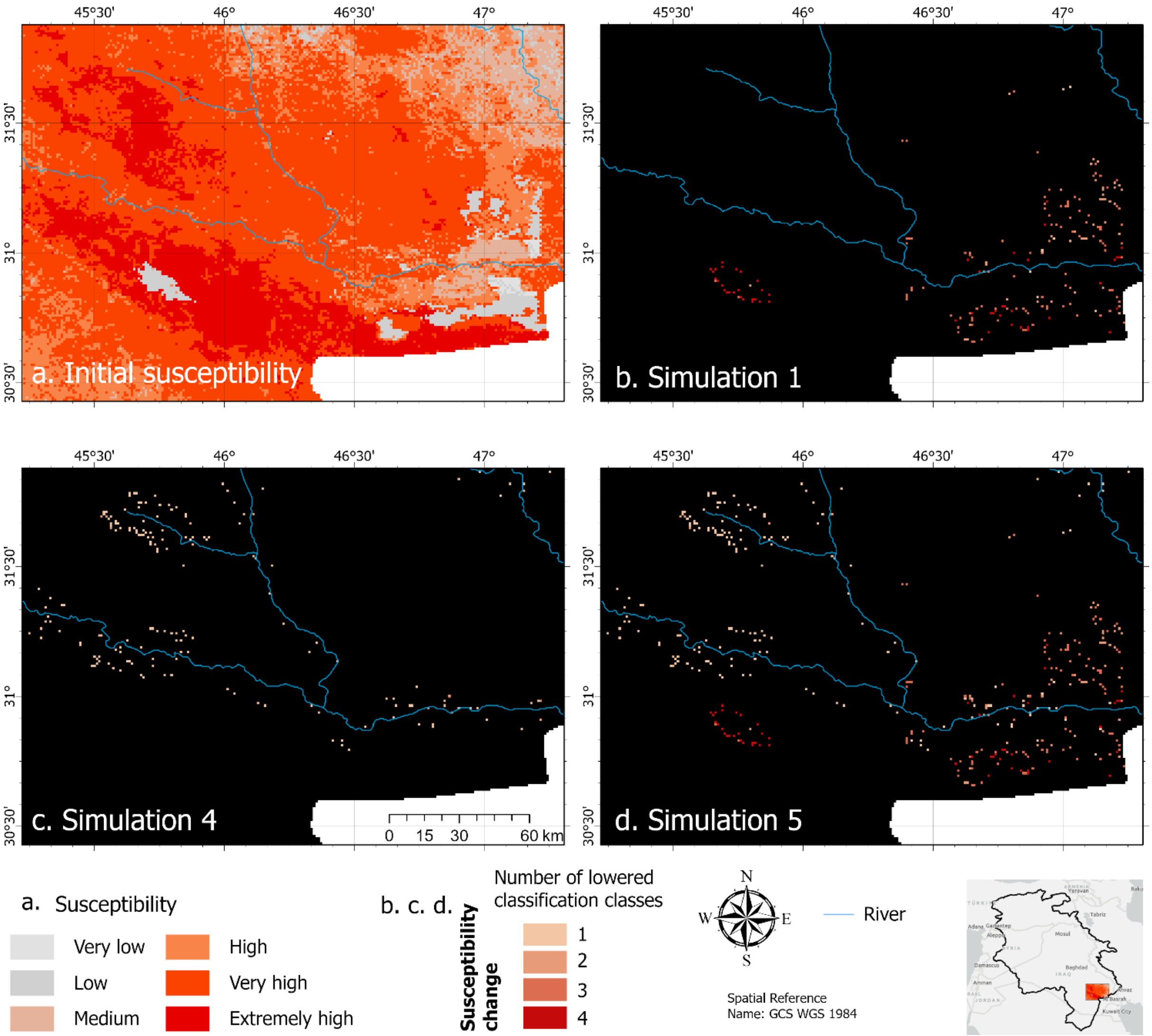

Figure 20. Spatial analysis results for susceptibility change for Area 3: a. initial susceptibility map in 2020, b. susceptibility class changes following the Lake Expansion, Simulation 1, c. susceptibility class changes following the Combined Land Use Change, Simulation 4, and d. susceptibility class changes following combined Lake Expasion and Land Use Changes, Simulation 5.

Figure 20 shows a visual representation of the changes in susceptibility classification between the original susceptibility map from 2020 (*Figure 20a*) and the applied simulations. The Lake Expansion simulation (Simulation 1, *Figure 20b*) shows an overall stronger effect on the susceptibility of the affected pixels than the Combined LUC, Simulation 4 (*Figure 20c*). In fact, Simulation 4 showed a maximum of 2 classes drop, while Simulation 1 included a 4 class drop at numerous locations. There are two clusters in the western regions that were more substantially affected by Simulation 4 (*Figure 20c*). This shows that central and eastern regions of *Area 3* are not responding strongly to both simulations. The stronger impact of Simulation 1 on the region is clearly visible in *Figure 20d*.

Area 3 - local effect

Table 20. Relative local effectiveness statistics for Area 3 simulations 1 to 5.

Susceptibility Map	*Mask name*	*Mask area (km²)*	*Buffer area (km²)*	*Affected*	*Mean susc.*	*Mean improv.*	*High+ classes*	*Classif. Improv.*	*Neighbour effect (Spatial Model)*
Original	Lakes	290	4910	5.91%	0.723		89.82%		
Simulation 1					0.704	2.58%	85.91%	3.91%	No
Original	Cropland	290	5991	5.19%	0.708		84.94%		
Simulation 2					0.706	0.27%	84.67%	0.27%	No
Original	Natural vegetation	314	5007	6.27%	0.709		82.98%		
Simulation 3					0.706	0.42%	82.82%	0.16%	No
Original	Cropland + vegetation	604	10598	5.70%	0.708		84.02%		
Simulation 4					0.708	0.04%	83.80%	0.22%	No
Original	Lakes + LUC	894	14017	6.38%	0.719		86.78%		
Simulation 5					0.711	1.16%	85.25%	1.53%	No

Locally, *Area 3* responded best to the lake expansion simulation (see *Table 20*). The simulation that produced the least improvement in the classification was the LUC from bare soil to natural vegetation (Simulation 3). The simulation that showed the least improvement in the mean susceptibility value was the Cropland simulation 2. Thus, making the LUCs the least effective strategies in *Area 3*. The application of the *Spatial Model* did not influence the masks' neighbouring pixels in any of the simulations.

Area 3 - regional effect

Table 21. Relative regional effectiveness statistics for Area 3 simulations 1-5.

Susceptibility Map	***Mask area (km²)***	***Total area (km²)***	***Affected***	***Mean susc.***	***Mean improv.***	***High+ classes***	***Classif. Improv.***
Original	-	34993	-	0.739	-	89.89%	-
Simulation 1	290		0.83%	0.737	0.35%	89.33%	0.55%
Simulation 2	290		0.83%	0.749	0.04%	89.84%	0.04%
Simulation 3	314		0.90%	0.739	0.06%	89.86%	0.02%
Simulation 4	604		1.73%	0.738	0.10%	89.82%	0.07%
Simulation 5	894		2.55%	0.736	0.45%	89.27%	0.61%

Regionally, as seen in *Table 21*, the simulations including lake expansions (Simulation 1 and Simulation 5) had the most pronounced effect on the whole region in terms of lowering the overall susceptibility and the proportion of High+ classes. Simulation 2, 3 and 4 did not cause any largely noticeable difference in the mean or the count of High+ classes. In fact, Simulation 2 recorded only a 4 km^2 and 43 km^2 fall from the Extremely High and Very High classes respectively. Simulation 3 downgraded 68 km^2 of the Extremely High classes. When checking the counts for each individual class in the simulations result, it became apparent that due to Simulation 4, 87 km^2 were downgraded from the highest susceptibility classes, where 72 km^2 dropped out of the Extremely High category.

Comparing the mean susceptibility values and the distribution of High+ classes between the study areas shows a pronounced difference between Area 3 and the other two regions. Area 3 contain over 89% High+ classes, while *Area 2*, despite having a slightly higher mean susceptibility has 10% less High+ classes than *Area 1*. This suggests a larger amount of highly susceptible classes in *Area 2* as compared to *Area 1*.

4.3. Simulations effectiveness

Using the Intensity of Change (IOC) metric introduced in the 'Evaluation metrics' section, the local and regional effectiveness of simulations is compared in *Table 22* below. The results were ordered by the Classification IOC value, with the most effective simulations at the top.

Table 22. The comparison between all simulations' effectiveness on local and regional scales, ordered by the largest Classification Intensity of Change value.

	Local			Regional	
Simulation	*Mean IOC (%)*	*Class IOC (%)*	***Simulation***	*Mean IOC (%)*	*Class IOC (%)*
Area 1 – Strategy 3	0.6864	0.8332	**Area 2 – Strategy 5**	0.0255	0.0451
Area 2 – Strategy 1	0.3400	0.5352	**Area 1 – Strategy 4**	0.0164	0.0193
Area 2 – Strategy 3	0.2631	0.5216	**Area 2 – Strategy 4**	0.0093	0.0183
Area 2 – Strategy 5	0.2249	0.3586	**Area 3 – Strategy 5**	0.0115	0.0156
Area 1 – Strategy 4	0.3707	0.3060	**Area 1 – Strategy 3**	0.0078	0.0110
Area 3 – Strategy 1	0.1523	0.2310	**Area 2 – Strategy 3**	0.0051	0.0107
Area 2 – Strategy 4	0.1057	0.1820	**Area 3 – Strategy 1**	0.0029	0.0045
Area 3 – Strategy 5	0.0739	0.0974	**Area 2 – Strategy 1**	0.0023	0.0034
Area 1 – Strategy 2	0.1448	0.0625	**Area 1 – Strategy 2**	0.0015	0.0012
Area 2 – Strategy 2	0.0251	0.0331	**Area 3 – Strategy 4**	0.0017	0.0011
Area 3 – Strategy 4	0.0195	0.0124	**Area 2 – Strategy 2**	0.0051	0.0010
Area 3 – Strategy 2	0.0142	0.0139	**Area 3 – Strategy 2**	0.0003	0.0004
Area 3 – Strategy 3	0.0262	0.0100	**Area 3 – Strategy 3**	0.0005	0.0002

All IOC values show that LUC simulations (Simulation 2,3 and 4) are not very effective in *Area 3*. These were found in the bottom four results for both regional and local scales. Regionally, the most effective simulation was the combined lake and LUC Simulation 5 in *Area 2*, followed by the combined LUC simulation in *Area 1*. Locally, the most effective strategy was natural vegetation expansion in *Area 1* followed by the lake expansion in *Area 2*. Analogously to what was presented before, the lakes expansion simulations have the strongest effect in *Area 3*, both locally and regionally. While the bottom five simulations align for both IOC metrics, the top three do not.

5. Discussion

This discussion aims to analyse and interpret the key findings, draw meaningful conclusions, and explore their implications in the broader context. It begins with a discussion relating to the *Pixel Model's* original susceptibility maps for all study areas. It moves on to discuss the results of the simulations and the impact of the *Spatial Model* on neighbouring pixels in the classification. The last segment of the discussion addresses the assumptions and limitations that have impacted this project, both in terms of modelling and control strategies.

Original susceptibility maps

The original susceptibility maps show a few spatial patterns that are supported by previous research, but also a few that differ from previous findings. For example, the susceptibility map created by Boloorani et al. (2022), places the hot spots at the Iraq-Iranian border in the south-east and in the central-western TERB, by the Syrian-Iraq border. While these areas show high susceptibility with some hot spots, the area with highest susceptibility region as seen in *Figure 13* is in the southern TERB, around Euphrates River and Gharraf Canal. One possibility for the south-eastern TERB showing a lower susceptibility in this study could be the afforestation strategy undertaken by the Kuwait Institute of Scientific Research (Al-Dousari et al., 2022) already producing an effect by 2020. The presence of hot spots near the borders further highlights the transboundary context of mitigating dust storms (Bremer, 2016, Middleton & Kang, 2017) and the necessity for international cooperation, both scientifically and politically.

Out of the three study areas, *Area 1*, which is located at the Syrian-Iraq border, identified as a hot spot by Boloorani et al. (2022), shows the lowest mean susceptibility classification at 0.579, followed by *Area 2* 's 0.593 and *Area 3*'s significantly higher 0.739. The apparent relationship between low susceptibility and presence of river becomes less pronounced downstream of Euphrates River, disappearing almost completely in the southern TERB. As described in the 'Background' section, many researchers point to the importance of water mismanagement in the continually increasing dust storm frequency (e.g., Maleki et al., 2021, Salehi et al., 2021, Middleton et al., 2019). One possibility, in line with Bremer's (2016) findings, is that the creation of more dams upstream of Euphrates and Tigris limited the amount of water available for agriculture, which coupled with insufficient use of irrigation water in the north caused water shortages in the southern regions. This finding is especially important as 2020 was a wet year and *Area 3* experienced the highest natural vegetation land cover (*Table 9* – 'Methods'), and rainfall from all three regions (*Table 4* – 'Methods'). However, agricultural practices are not the only issue present in the region that might be causing the increased susceptibility in the south. *Area 3* includes a number of lakes and wetlands, which have been documented to partially dry out and cause an increase in dust storm frequencies (Boloorani et al., 2022, Naghibi et al., 2023).

Local susceptibility

One of the more interesting findings from *Area 2* presents with an average susceptibility 5 km around the lakes equal to 0.643 (*Table 18*), while the region's susceptibility is 0.593 (*Table 19*). Showing such an increase in dust source susceptibility supports previous research outcomes stating that increasingly more dust storm sources in the TERB are found in the vicinity of the lakes (Boloorani et al., 2022, Naghibi et al., 2023). Only *Area 2's* lake buffer showed such an increase, while all other local buffer areas showed slightly lower susceptibilities at all other the study localities (*Table 16* for *Area 1, Table 20* for *Area 3*).

Another finding from *Area 2* showed that there appears to be little influence of the applied strategies on medium susceptibility areas (as seen in *Figure 18a* compared with *18c*). The effectiveness of the simulation is much stronger in the High+ classes, however, *Area 1* showed a single class drop in more Medium susceptibility classes (*Figure 17b*), highlighting a possible link between the simulation's effectiveness and other spatial effects and conditions. *Area 3* additionally shows less and smaller class changes for the LUC simulations than the other areas.

Statistical analysis findings

The statistical analysis of the simulation results for dust control strategies involved two types of metrics. The first type focused on relative improvement and measured the percentage decrease in two aspects: 1) the mean susceptibility value, and 2) the distribution of the High+ classes. These metrics assessed the extent of improvement relative to the initial values. The second metric examined the intensity of change (IOC) of the first metric between the applied simulations and the initial susceptibility. It captured the overall effectiveness across all the simulations and regions. Coupling the analysis of the changes in individual pixels' classification with the statistical metrics provided enough information to form initial observations on the simulations' effectiveness and their spatial distribution.

All 13 simulations performed in the study showed a decrease in the mean susceptibility and a drop in the number of High+ classes. The strongest effects are seen in *Area 1* and *Area 2*, with the least effective strategy being the cropland expansion. *Area 3*′s LUC simulation had very little effect on the susceptibility, unlike the lake expansion simulations. Locally, Simulation 1 was more effective for *Area 2* than *Area 3*, however, regionally the opposite was observed. Overall, *Area 1* and *Area 2* results are more similar than the results for *Area 3*. A larger number of affected pixels did not change the classification in Area 3, which shows in the IOC table (*Table 22*).

Looking back at the 'Dynamic variables' and 'Data analysis and preparation' sections, some facts about the underlying conditions in *Area 3* become apparent. In 2020, this area experienced the most rainfall (*Table 4*), had the highest coverage of natural vegetation at 45% (*Table 9*), and highest average NDVI (*Table 7*). Additionally, the most common soil type in the area was Sandy Clay Loam (*Figure 7a*), which is the third most strongly associated soil type with the dust sources in the TERB (*Figure 7c*). At first glance, these environmental conditions appear to favour lower dust storm susceptibility (higher NDVI, natural vegetation cover and precipitation), but as can be seen from the susceptibility mapping and statistical results, the overall susceptibility in the area is much higher than in the other two regions. This strongly suggests that there are underlying patterns in this area, that are not present in Area 1 or Area 2 that should be investigated in future research. *Table 9* shows that the second most common land cover with the most dust sources in the area is the natural vegetation class, which covers 45% of the area. Perhaps, there are potential feedback mechanisms that affect the susceptibility and response to the mitigation strategies. A further detailed analysis is needed that would consider these region-specific factors, specifically focusing on land cover as the region is rich in marshes.

Hypotheses

The findings of this study support the hypothesis that the application of dust storm control strategies would lead to an overall decrease in the area's dust source susceptibility, as observed through the analysis of the change detection maps (*Figure 17*, *18*, and *20*) and the improvement metrics (*Table 16-21)*. Specifically, the simulations result consistently showed a decrease in susceptibility across all the study areas, for all strategies, albeit by an occasionally very small amount, especially when considering LUC simulations in *Area 3*. Visual interpretation of the results has shown that each area experienced a 1 to 4 classes drop, which amounts to a minimum of ~0.01% and maximum ~59.99% decrease in the pixel's susceptibility to forming dust storms. From the visual inspection of the lake simulations effectiveness (*Figures 18b and 20b*), compared to the LUCs *(Figures 17b, 18c and 20c*), it becomes apparent that the drop of the susceptibility class per pixel is more consistent and stronger at the lake's expansion sites. This finding supports previous research suggestions that improving water management practices will have a positive impact on decreasing dust storm frequency (Naghibi et al., 2023, Boloorani et al., 2022, Maleki et al., 2021, Salehi et al., 2021, Middleton et al., 2019). As such, Hypothesis I was accepted, with recommendations for subsequent research and analysis.

Due to the spatial nature of dust storms and their formation, it was hypothesised that including a neighbourhood effect in susceptibility mapping would improve the results by affecting the classification of the pixels surrounding the simulation mask. The *Spatial Model* was developed to test this hypothesis. It was an adapted version of the *Pixel Model* that included the neighbourhood effect in the input values selection. However, the findings of this study indicate that including a spatial effect in susceptibility mapping does not impact the susceptibility classification of the pixels surrounding the simulation mask. Contrary to the initial hypothesis, the analysis revealed no changes in the susceptibility classification, outside of the pixels affected by the mask (see example in *Figure 19*). This phenomenon could be attributed to the insufficient influence of the neighbourhood effect, or human error in the creation of the algorithm and therefore Hypothesis II is conditionally rejected, pending more algorithm testing. Perhaps the algorithm does not sufficiently amplify the neighbouring values to impact the classification. A possible improvement to the hypothesis would be to include the neighbouring effect in the simulations of the input variables themselves, rather than only in the susceptibility mapping model.

Spatial patterns

Looking at the visual simulation effectiveness shown in *Figures 17-18 and Figure 20*, compared with the results presented in *Table 22*, it becomes clear that *Area 1* and *Area 2* had a stronger response to the dust control strategies than *Area 3*. Particularly regarding the LUC strategies. *Area 3* has seen close to no improvement in the susceptibility for these simulations at both scales and an increase of the mean susceptibility value as mentioned previously for Simulation 4. Notably, *Figure 20c* reveals an interesting observation, where a substantial portion of the cropland mask pixels and some vegetation mask pixels in *Area 3* exhibited no change in their susceptibility classification. This phenomenon was also present in other LUC simulations conducted in *Area 1* and *Area 2*, but it was not as pronounced. Several factors may account for this outcome, including the statistical values derived from the land use and soil type variables (please refer to *Appendix 1*). These values may be accurate, meaning that other factors are influencing the area's susceptibility more than the updated dynamic variables. Conversely, they may inadequately represent reality due to the potentially limited amount of soil types and land uses available for the analysis in the area. Regardless, this finding presents a valuable opportunity for further investigation and research. The top two strategies for *Area 3* were the lake expansion and the combined lake expansion and LUC strategies (*Figure 18b, 20d, Table 21*). This highlights the importance of adjusting each strategy to the locally affected areas, as they do not respond to the strategies in the same manner. This finding supports Park et al.'s (2020) assessment that adaptation ability in each region plays a crucial role in the formation and development of dust storms. To further improve on these findings, it is suggested to perform a thorough analysis on the locations where the positive effects are clustered (such as in the western region of *Area 3*) versus the areas with very little effect (such as the central part of *Area 3 – Figure 20d*).

Factors limitations

One of the major limitations of this study is that it only considers environmental factors and does not include more anthropogenic factors, other than cropland and urban land use classes. With the formation of new dust sources being increasingly linked to human activity (Papi et al., 2022, Middleton et al., 2019) a more in-depth analysis and inclusion of anthropogenic factors might be required to formulate effective dust storm mitigation strategies. Another relevant limitation is the lack of local community and environmental knowledge in the creation of the control strategies for this project. These kinds of simulations would benefit from local knowledge to create more realistic results and to potentially help in addressing the political and scientific disconnect, as mentioned by Saleki et al. (2021) and Amiraslani and Dragovich (2011).

Assumptions and limitations

The assumption of stationarity was the most important assumption made when creating the dataframe for the XGBoost model that was based on 20 years of data. It was assumed that the relationship between the predictor variables and the target remain consistent over time. An assumption was also made that susceptibility mapping will effectively represent the influence of control strategies on dust source formation. However, susceptibility mapping itself is also subject to several limitations. Primarily, the accuracy and reliability of the model are dependent on the quality of the input data. Despite diligent efforts to collect high-quality data from reliable sources, inherent limitations or uncertainties associated with the data collection process, such as potential measurement errors or inconsistencies may still exist. There is a potential for error due to the majority of dust sources being present in small regions in *Area 3*, which may have skewed the model results. Additionally, due to this project's complexity and reliance on many code scripts, there is a potential for human error, despite steps being taken to minimize it, through thorough quality checks.

With regards to the simulations, several assumptions and limitation were present. In the lake expansion scenario, an assumption was made that partial opening of the dams along the Euphrates and Tigris rivers will lead to an increase in water flow, benefiting downstream lakes that are fed by these rivers. Another assumption was the use of a uniform, random expansion of the lake size by 20% in both study areas, that does not follow any specific spatial pattern or depend on the underlying topography. The final assumption was that expanding the lake size will have a direct impact on soil moisture, soil evaporation and NDVI values. However, the simulation simplifies the complex dynamics of water management and the impacts of dam operations, focusing only on the general assumption of increased water flow. Another limitation was that all the simulations rely heavily on the available data sources for lake size, soil moisture, soil evaporation and the NDVI, which have inherent limitation and uncertainties. Finally, the choice of 20% expansion of the lake size was based on an assumption and lacks specific empirical evidence.

In the LUC strategies, the assumption was made that establishing cropland is more feasible within a 5 km distance from the river due to easier access to water resources and suitable soil conditions. Furthermore, an assumption was made that natural vegetation can be more easily established further away from the river (5-10 km) compared to cropland. The final assumption was that changing land cover classes from bare soil to cropland or natural vegetation will have a direct impact on soil moisture, soil evaporation and NDVI values, and that these values can be statistically evaluated from the available data. This, however, provides a set of limitations, as these simulations rely heavily on the statistical analysis for determining the values to be changed based on soil texture, assuming it represents the actual changes that would occur in the field. LUCs simulations also simplify complex land use dynamics, by not considering other factors that might affect land cover changes, such as land ownership, land management practices and socio-economic constraints.

This project has the potential to serve as a starting point for further research into understanding and modelling the effects of dust storm mitigation strategies around the world. As the results have clearly shown, the effectiveness of a dust control strategy was strongly depended on the study area. Consequently, any future studies should carefully consider which factors and areas should be targeted that have the potential to influence dust source formation in the region. To ensure realistic results, local community knowledge and environmental assessment should be considered when deciding on the strategies. To build on the current project, it is recommended to expand the buffer zones and increase the magnitude of changes to the areas to check if the theoretical impact would increase. Additional research is also recommended with regards to the spatial patterns in the decrease of susceptibility classes. As these represented a decrease between ~0.01% to ~59.99% per pixel, it potentially might paint a different picture regarding the effectiveness of the strategies, than the statistical analysis presented in this study. It is therefore crucial to consider both results when assessing the effectiveness of dust control strategies.

6. Conclusion

Through dust source susceptibility mapping, this project aimed to simulate dust storm control strategies using XGBoost machine learning models and to evaluate their impacts based on simulation results. The study's original susceptibility maps revealed spatial patterns consistent with previous research but also some differences. Dust source hot spots were observed near the Iraq-Iranian and Syrian-Iraq borders, highlighting the transboundary nature of dust storm mitigation and the need for international cooperation. *Area 1*, located at the Syrian-Iraq border, showed the lowest overall susceptibility, while *Area 3* in the southern TERB had the highest overall susceptibility.

The results supported previous research and highlighted the importance of efficient water management practices to mitigate increasing dust storm formations at the locations of drying lakes and wetlands. The findings upheld the initial hypothesis that dust storm control strategies would decrease the area's overall susceptibility. All of the applied simulations consistently showed a decrease in susceptibility and in the count of high susceptibility classes across all study areas. The effectiveness of the strategies varied depending on the region and the specific strategy employed.

The study revealed a regionally varied response to the simulation strategies, with *Area 1* and *Area 2* showing stronger reactions compared to *Area 3*. The bare land to natural vegetation LUC was found to be the most effective local strategy in *Area 1*. In *Area 2* and *Area 3*, the expansion of the lakes had the strongest local impact, reducing overall susceptibility and visibly decreasing high susceptibility classifications. The least effective strategy across all the areas was the cropland expansion.

Additionally, the application of the *Spatial Model* did not yield any noticeable impact on neighbouring pixels, leading to the conditional rejection of the second hypothesis. This lack of impact may be attributed to issues with the algorithm, or insufficient magnitude of changes to cause classification differences in the model. Future research should prioritize the implementation of spatial effects within the control strategies themselves, rather than solely focusing on incorporating the effect in the susceptibility mapping model. A study to compare the *Pixel* and *Spatial Model* is also recommended to ascertain advantages and disadvantages in both approaches.

The limitations of the study included the lack of consideration for anthropogenic factors, potential for human error and the absence of local community and environmental knowledge in formulating the strategies. The inclusion of these factors could improve the effectiveness of dust storm mitigation strategies. Assumptions were made regarding stationarity, data quality and the impact of control strategies on susceptibility mapping. Limitations were present in the simulation assumptions, such as the uniform expansion of lake size and reliance on available data sources. The choice of parameters, such as the 20% expansion of the lake size, lacked specific empirical evidence and should be addressed in future studies.

In summary, this project has the potential to serve as a starting point for further research into understanding and modelling the effects of dust storm mitigation strategies. The findings support the effectiveness of the strategies in decreasing dust source susceptibility, but further research is needed that would consider anthropogenic factors and improve the incorporation of spatial effects. Addressing the limitations and refining the models can also contribute to more effective dust storm mitigation strategies in the future.

References

Amiraslani, F., & Dragovich, D. (2011). Combating desertification in Iran over the last 50 years An overview of changing approaches. *Journal of Environmental Management*, *92*(1), 1-13. https://doi.org/10.1016/j.jenvman.2010.08.012

Azoogh, L., Moghadam, B. K., & Jafari, S. (2018). Interaction of petroleum mulching, vegetation restoration and dust fallout on the conditions of sand dunes in southwest of Iran. *Aeolian Research, 32,* 124-132. https://doi.org/10.1016/j.aeolia.2018.01.007

Al-Dousari, A., Omar, A., Al-Hemoud, A., Aba, A., Alrashedi, M., Alrawi, M., Rashki, A., Petrov, P., Ahmed, M., Al-Dousari, N., Baloshi, O., Jarba, M., Esmail, A., Alsaleh, A., & William, T. (2022). A Success Story in Controlling Sand and Dust Storms Hotspots in the Middle East. *Atmosphere*, *13*(8). https://doi.org/10.3390/atmos13081335

Al-Madhhachi, A. S. T., Rahi, K. A., & Leabi, W. K. (2020). Hydrological Impact of Ilisu Dam on Mosul Dam; the River Tigris. *Geosciences*, *10*(4). https://doi.org/10.3390/geosciences10040120

Awadh, S.M. (2023). Impact of North African Sand and Dust Storms on the Middle East Using Iraq as an Example: Causes, Sources, and Mitigation. *Atmosphere*,*14(1),* 180, doi: https://doi.org/10.3390/atmos14010180

Bakr, N., & Afifi, A. A. (2019). Quantifying land use/land cover change and its potential impact on rice production in the Northern Nile Delta, Egypt. *Remote Sensing Applications-Society and Environment*, *13*, 348-360. https://doi.org/10.1016/j.rsase.2018.12.002

Boloorani, A. D., Kazemi, Y., Sadeghi, A., Shorabeh, S. N., & Argany, M. (2020). Identification of dust sources using long term satellite and climatic data: A case study of Tigris and Euphrates basin. *Atmospheric Environment*, *224*. https://doi.org/10.1016/j.atmosenv.2020.117299

Boloorani, A. D., Papi, R., Soleimani, M., Karami, L., Amiri, F., & Samany, N. N. (2021). Water bodies changes in Tigris and Euphrates basin has impacted dust storms phenomena. *Aeolian Research*, *50*. https://doi.org/10.1016/j.aeolia.2021.100698

Boloorani, A. D., Samany, N. N., Papi, R., & Soleimani, M. (2022). Dust source susceptibility mapping in Tigris and Euphrates basin using remotely sensed imagery. *Catena*, *209*. https://doi.org/10.1016/j.catena.2021.105795

Boroughani, M., Pourhashemi, S., Hashemi, H., Salehi, M., Amirahmadi, A., Asadi, M. A. Z., & Berndtsson, R. (2020). Application of remote sensing techniques and machine learning algorithms in dust source detection and dust source susceptibility mapping. *Ecological Informatics*, *56*. https://doi.org/10.1016/j.ecoinf.2020.101059

Bremer, N. C. (2016). Transboundary Environmental Impact Assessment of Large Dams in the Euphrates-Tigris Region: An Analysis of International Law Binding Iran, Iraq, Syria and Turkey. *Review of European Comparative & International Environmental Law*, *25*(1), 92-106. https://doi.org/10.1111/reel.12145

Brownlee, J. (2020). Handling Categorical Data in Machine Learning: The One-Hot Encoding Guide. *Machine Learning Mastery*. https://machinelearningmastery.com/one-hot-encoding-for-categorical-data/

Can, R., Kocaman, S., & Gokceoglu, C. (2021). A Comprehensive Assessment of XGBoost Algorithm for Landslide Susceptibility Mapping in the Upper Basin of Ataturk Dam, Turkey. *Applied Sciences-Basel*, *11*(11). https://doi.org/10.3390/app11114993

Chen, T. & Guestrin, C. (2016). XGBoost. Proceedings of the 22nd ACM SIGKDD International Conference on Knowledge and Discovery and Data Mining. https://doi.org/10.1145/2939672.2939785

Didan, K. (2021). MODIS/Terra Vegetation Indices 16-Day L3 Global 1km SIN Grid V061 [Data set]. *NASA EOSDIS Land Processes DAAC*. https://doi.org/10.5067/MODIS/MOD13A2.061

FAO (2009) Transboundary River Basin Overview – Euphrates-Tigris. *FAO Aquastats Reports,* https://www.fao.org/3/CA2132EN/ca2132en.pdf

Friedman, J.H. (2001). Greedy function approximation: a gradient boosting machine. *The Annals of Statistics 29(5).* https://doi.org/10.1214/aos/1013203451

Friedl, M., Sulla-Menashe, D. (2022). MODIS/Terra+Aqua Land Cover Type Yearly L3 Global 500m SIN Grid V061 [Data set]. *NASA EOSDIS Land Processes DAAC*. https://doi.org/10.5067/MODIS/MCD12Q1.061

Gan, R., Zhang, Y.Q., Shi, H., Yang, Y.T., Eamus, D., Cheng, L., Chiew, F.H.S., Yu, Q., (2018). Use of satellite leaf area index estimating evapotranspiration and gross assimilation for Australian ecosystems. *Ecohydrology*, https://doi.org/10.1002/eco.1974

Géron, A. (2019). *Hands-on machine learning with Scikit-Learn, Keras, and TensorFlow*. O'Reilly Media, Inc.

Gholami, H., Mohamadifar, A., & Collins, A. L. (2020). Spatial mapping of the provenance of storm dust: Application of data mining and ensemble modelling. *Atmospheric Research*, *233*. https://doi.org/10.1016/j.atmosres.2019.104716

Ginoux, P., Prospero, J. M., Torres, O., & Chin, M. (2004). Long-term simulation of global dust distribution with the GOCART model: correlation with North Atlantic Oscillation. *Environmental Modelling & Software*, *19*(2), 113-128. https://doi.org/10.1016/S1364-8152(03)00114-2

Guyon, I., & Elisseeff, A. (2003). An introduction to Variable and Feature Selection. *Journal of Machine Learning Research, 3,* 1157-1182.

Han, Q., Zeng, Y., Zhang, L. et al. (2023). Global long term daily 1 km surface soil moisture dataset with physics informed machine learning. *Sci Data 10(101).* https://doi.org/10.1038/s41597-023-02011-7

Huffman, G.J., E.F. Stocker, D.T. Bolvin, E.J. Nelkin, Jackson Tan (2019), GPM IMERG Final Precipitation L3 1 month 0.1 degree x 0.1 degree V06, Greenbelt, MD, *Goddard Earth Sciences Data and Information Services Center (GES DISC)*, https://doi.org/10.5067/GPM/IMERG/3B-MONTH/06

Khalilimoghadam, B., Jamili, T., Nadian, H., Shahbazi, E., (2015), The influence of sugarcane mulch on sand dune stabilization in Khuzestan, the southwest of Iran. *Iran Agricultural Research 34,* 71-80.

Lehner, B., Grill G. (2013). Global river hydrography and network routing: baseline data and new approaches to study the world’s large river systems. *Hydrological Processes*, *27(15)*, 2171–2186. https://doi.org/10.1002/hyp.9740

Maleki, S., Miri, A., Rahdari, V., & Dragovich, D. (2021). A method to select sites for sand and dust storm source mitigation: case study in the Sistan region of southeast Iran. *Journal of Environmental Planning and Management*, *64*(12), 2192-2213. https://doi.org/10.1080/09640568.2020.1862770

Middleton, N., & Kang, U. (2017). Sand and Dust Storms: Impact Mitigation. *Sustainability*, *9*(6). https://doi.org/10.3390/su9061053

Middleton, N., Tozer, P., & Tozer, B. (2019). Sand and dust storms: underrated natural hazards. *Disasters*, *43*(2), 390-409. https://doi.org/10.1111/disa.12320

Ministry of Environment of Iraq (2013). The National Environmental Strategy and Action Plan of Iraq. https://www.unep.org/resources/report/national-environmental-strategy-and-action-plan-2013-2017-iraq

Mutasher, A. K. A., Al-Mohammed, F. M., & Aljibori, H. S. S. (2021). Groundwater Quality Assessment for Irrigation Purpose Using Water Quality Index in Green Belt Project in Karbala City-Iraq. *Journal of Engineering Science and Technology*, *16*(5), 4060-4078. https://WOS:000722952500030

Namdar-Khojasteh, D., Bazgir, M., Hashemi Babaheidari, S. A., & Asumadu-Sakyi, A. B. (2022). Application of biocementation technique using Bacillus sphaericus for stabilization of soil surface and dust storm control. *Journal of Arid Land*, *14*(5), 537-549. https://doi.org/10.1007/s40333-022-0017-9

Naghibi, A., Hashemi, H., Zhao, P., Brogaard, S., Eklund, L., Hassan, H.H., Mansourian, A. (2023). *Spatiotemporal variability of dust source susceptibility during wet and dry periods: The Tigris-Euphrates River Basin*. [Manuscript submitted for publication], Centre for Advanced Middle Eastern Studies, Lund University

Newman, D.A. (2014). Missing data: Five practical guidelines. *Organizational Research Methods*, 17(4), pp.372–411.

Papi, R., Attarchi, S., Boloorani, A. D., & Samany, N. N. (2022). Characterization of Hydrologic Sand and Dust Storm Sources in the Middle East. *Sustainability*, *14*(22). https://doi.org/10.3390/su142215352

Park, E., Kim, J., Song, C., Jo, H. W., Lee, S., Kim, S. J., Park, S., Lim, C. H., & Lee, W. K. (2020). Applicability Analysis of Vegetation Condition and Dryness for Sand and Dust Storm (SDS) Risk

Reduction in SDS Source and Receptor Region. *Sustainability*, *12*(18). https://doi.org/10.3390/su12187256

Pedregosa, F., Varoquaux, G., Gramfort, A., Michel, V., Thirion, B., Grisel O., Vanderplas, J. (2011). Scikit-learn: Machine learning in Python. *Journal of Machine Learning Research 12(10),* 2825-2830.

Pourhashemi, S., Asadi, M. A. Z., Boroughani, M., & Azadi, H. (2022). Mapping of dust source susceptibility by remote sensing and machine learning techniques (case study: Iran-Iraq border). *Environmental Science and Pollution Research*. https://doi.org/10.1007/s11356-022-23982-x

Salehi, S., Ardalan, A., Ostadtaghizadeh, A., Zareiyan, A., Garmaroudi, G., & Rahimiforoushani, A. (2021). Strategies and experiences for sand and dust storm adaptation: A qualitative study in Iran. *Journal of Environmental Health Science and Engineering*, *19*(2), 1753-1763. https://doi.org/10.1007/s40201-021-00730-w

Tan, M. H., & Li, X. B. (2015). Does the Green Great Wall effectively decrease dust storm intensity in China? A study based on NOAA NDVI and weather station data. *Land Use Policy*, *43*, 42-47. https://doi.org/10.1016/j.landusepol.2014.10.017

UNDP (2022). Updating Iraq's National Environmental Strategy and Action Plan (NESAP) https://www.undp.org/iraq/stories/updating-iraqs-national-environmental-strategy-and-action-plan-nesap

Wang, X. M., Zhang, C. X., Hasi, E., & Dong, Z. B. (2010). Has the Three Norths Forest Shelterbelt Program solved the desertification and dust storm problems in arid and semiarid China? *Journal of Arid Environments*, *74*(1), 13-22. https://doi.org/10.1016/j.jaridenv.2009.08.001

XGBoost, (2022) XGBoost Documentation. https://xgboost.readthedocs.io/en/stable/

Yesilnacar, E. K. (2005). *The Application of Computational Intelligence to Landslide Susceptibility Mapping in Turkey*. University of Melbourne, Department 200.

Yokoya,N., Yamanoi, K., He, W., Baier, G., Adriano, B., Miura, H., and Oishi, S. (2022). Breaking Limits of Remote Sensing by Deep Learning from Simulated Data for Flood and Debris-Flow Mapping. *IEEE Transactions on Geoscience and Remote Sensing, 60,* 1-15, https://doi.org/10.1109/TGRS.2020.3035469

Zhang, Y., Kong, D., Gan, R., Chiew, F.H.S., McVicar, T.R., Zhang, Q., and Yang, Y., (2019). Coupled estimation of 500m and 8-day resolution global evapotranspiration and gross primary production in 2002-2017. Remote Sensing of Environment. *222 (1),* 165-182, https://doi.org/10.1016/j.rse.2018.12.031

Zhang, Y., Peña-Arancibia, J.L., McVicar, T.R., Chiew, F.H.S., Vaze, J., Liu, C., Lu, X., Zheng, H., Wang, Y., Liu, Y.Y., Miralles, D.G., Pan, M., (2016). Multi-decadal trends in global terrestrial evapotranspiration and its components. *Scientific Reports*. *6*, 19124. https://doi.org/10.1038/srep19124

Appendices

Appendix 1. Scaling factors for Simulation 2, Simulation 3 and the combined Simulation 4. Affecting the values of soil moisture, NDVI and soil evaporation, depending on the soil texture type.

Bare Soil to Cropland, Simulation 2							
		Sandy Loam	*Sand*	*Loamy Sand*	*Loam*	*Sandy Clay Loam*	*Clay Loam*
Study Area 1							
	Soil moisture	1.13	1	1	1.06	1	1
	NDVI	1.8	1	1	2.54	1.55	1.33
	Soil evaporation	1.05	1	1	0.79	1	0.94
Study Area 2							
	Soil moisture	1.13	1	1	1.13	1.07	1.06
	NDVI	2.4	1	1	2.14	2.45	2.26
	Soil evaporation	1.13	1	1	0.85	0.97	0.77
Study Area 3							
	Soil moisture	1	1	1	1.06	1.15	1.07
	NDVI	1	1	1	1.33	1.82	1.31
	Soil evaporation	1	1	1	0.93	1.12	1.13

Bare Soil to Natural Vegetation, Simulation 3							
		Sandy Loam	Sand	Loamy Sand	Loam	Sandy Clay Loam	Clay Loam
Study Area 1							
	Soil moisture	1	0.93	1	1	1	0.94
	NDVI	1.3	1	1.3	1.36	1.44	1.25
	Soil evaporation	1.07	1.15	1.14	0.9	1.07	1
	Soil moisture	1.07	1.08	1	1	1.07	1
	NDVI	1.3	1.18	1.55	1.28	1.36	1.8
	Soil evaporation	1.13	1.56	1.13	0.97	1.13	0.088
	Soil moisture	1.08	1.08	1.08	1	1.08	1.07
	NDVI	1.55	1.22	1.37	1.13	1.45	1.31
	Soil evaporation	1.19	1.23	1.15	0.98	1.06	1.03